



# **Reconstruction of Partonic Substructure and Fragmentation of Jets in Heavy Ion Collisions at the LHC**

MASTERARBEIT

Master of Science

Physik

Eingereicht von:

Fabian Hordt

Angefertigt am:

Institut für Kernphysik, Westfälische Wilhelms-Universität Münster

Beurteilung:

Prof. Dr. C. Klein-Bösing (Betreuung)

Prof. Dr. A. Andronic

Münster, Juni 2021



---

# Contents

<b>1</b>	<b>Jet Evolution in a Medium</b>	<b>3</b>
1.1	The Strong Interaction . . . . .	3
1.2	Hot QCD Matter . . . . .	6
1.3	Hard Scattering and Factorisation . . . . .	7
1.3.1	Parton Distribution Functions . . . . .	8
1.3.2	Cross Section . . . . .	9
1.3.3	Fragmentation Functions . . . . .	9
1.4	Heavy Ion Collisions . . . . .	10
1.4.1	Nuclear Parton Distribution Functions . . . . .	10
1.4.2	Collision Geometry . . . . .	11
1.4.3	Evolution of the Quark Gluon Plasma . . . . .	13
1.5	Jet Energy Loss . . . . .	15
1.5.1	Collisional Energy Loss . . . . .	15
1.5.2	Radiative Energy Loss . . . . .	16
1.5.3	Higher Twist Energy Loss Model . . . . .	17
<b>2</b>	<b>Jets and Observables</b>	<b>19</b>
2.1	Substructure Observables . . . . .	22
2.2	The Lund Jet Plane . . . . .	23
2.3	Soft Drop . . . . .	26
2.4	Recursive Soft Drop . . . . .	27
2.5	Recoil Jets . . . . .	28
2.5.1	Recoil Jet Definition . . . . .	28
2.5.2	Recoil Observables . . . . .	29
<b>3</b>	<b>Computational Methods for Jet Observable Analyses</b>	<b>31</b>
3.1	PYTHIA 8.2 . . . . .	31
3.2	The JETSCAPE Framework . . . . .	33
3.3	Background Toy Model . . . . .	35
3.4	Analysis Tools . . . . .	35
<b>4</b>	<b>Evaluation of Analysis Routines</b>	<b>37</b>
4.1	Background Reduction for Jetshape Observables . . . . .	37
4.2	Recoil Jet Analysis with alternative FastJet Recombination Scheme . . . . .	43
4.2.1	Recoil Jet Spectra and $\Delta_{recoil}$ . . . . .	45
4.2.2	Angular Distribution and Large Angle Scattering . . . . .	51
4.3	Lund Plane Analysis with Background Toy Model . . . . .	55
<b>5</b>	<b>Summary and Outlook</b>	<b>59</b>

<b>A</b>	<b>Additional plots and tables</b>	<b>61</b>
A.1	Background Reduction for Jetshape Observables . . . . .	61
A.2	Recoil Jet Analysis with alternative FastJet Recombination Scheme . . . .	62
<b>B</b>	<b>How to JETSCAPE</b>	<b>65</b>
B.1	Installing JETSCAPE . . . . .	65
B.2	Running JETSCAPE . . . . .	67
B.3	Analysing JETSCAPE events . . . . .	68



---

# Acronyms

<b>ALICE</b>	a Large Heavy Ion Collider Experiment
<b>C/A</b>	Cambridge/Aachen
<b>CBM</b>	Compressed Baryonic Matter experiment
<b>CMS</b>	centre of mass
<b>DGLAP</b>	Dokshitzer-Gribov-Lipatov-Altarelli-Parisi
<b>DIS</b>	deep inelastic scattering
<b>FAIR</b>	Facility for Antiproton and Ion Research
<b>FF</b>	fragmentation function
<b>IRC</b>	infrared and collinear
<b>ISR</b>	initial state radiation
<b>LEP</b>	Large Electron-Positron collider
<b>LHC</b>	Large Hadron Collider
<b>LPM</b>	Landau-Pomeranchuk-Migdal
<b>ML</b>	machine learning
<b>MPI</b>	multiple parton interaction
<b>PDF</b>	parton distribution function
<b>nPDF</b>	nuclear parton distribution function
<b>QCD</b>	quantum chromo dynamics
<b>QED</b>	quantum electro dynamics
<b>QFT</b>	quantum field theory
<b>QGP</b>	quark gluon plasma
<b>RSD</b>	Recursive Soft Drop
<b>SM</b>	standard model of particle physics
<b>TT</b>	trigger track



---

# Introduction

In heavy ion collisions a reduced yield of jets is observed compared to proton-proton collisions, which is known as jet quenching. Since the first observations of jet quenching [1] in heavy ion collisions, the question was raised which underlying principles might explain the results. In the years since, a wide variety of observables were defined and measured to investigate the corresponding phenomena [2]. Despite those efforts most of the details of the underlying processes are still an open question and many different models of jet energy loss and the spacial and temporal evolution within the collisions exist [3]. Therefore it is still desired to define new observables which are more sensitive regarding the resolution of the various processes predicted by theory. One important aspect is to resolve the substructure of the jets in the early stages of collisions during which the outgoing partons fragment and interact with the coloured medium. This additionally raises the question whether the outgoing parton is initially a quark or a gluon.

This thesis aims to provide some further insights to the aforementioned aspects by evaluating the capabilities of different analysis routines which are currently used in terms of resolving of the jet substructure and the influence of the background of a heavy ion collision. The influence of Recursive Soft Drop (RSD) on the background in a jet, the differences between two recombination schemes concerning the angular distribution of hadron-jet correlations and the impact of combinatorial background on the *Lund plane* representation of jets are investigated using the PYTHIA [4] and JETSCAPE [5] Monte Carlo event generators. The thesis is structured as follows. In the first chapter the physics basics of heavy ion collisions are explained. The chapter starts with a short introduction to the strong interaction and follows up with all the effects which happen during the timeline of a heavy ion collision. Observables for the analysis of partonic jets are discussed in the second chapter. The focus lays on the observables which are regarded in this thesis. In the third chapter the computational methods for the analyses featured in this thesis are described and discussed. In the fourth chapter all analysis details and the results of the analyses are presented and discussed. This chapter is split into three main parts for the three different analysis tasks conducted in the scope of this thesis. Finally the last chapter gives a short summary and an outlook to the implications of the results. As there were many plots created for the different analysis steps, not all of them would fit into the main chapters, but they are shown in the appendix. Furthermore a short quick start manual for the JETSCAPE framework is supplied in Appendix B.

As common in particles physics natural units are used. In particular the speed of light  $c = 1$ .



---

# 1 Jet Evolution in a Medium

To develop a basic understanding of the underlying physics of the analysis, this chapter will provide a short introduction to the principles of the strong interaction, to the particular processes involved in high energy particle collisions and, based on the aforementioned, to the current understanding of the spatio-temporal evolution of scattered partons in a quark gluon plasma (QGP).

## 1.1 The Strong Interaction

The standard model of particle physics (SM) covers three of the four fundamental forces which shape everything we know. It covers the interaction of the elementary particles via the electromagnetic, via the weak, and via the strong interaction. All of these forces are formulated as a quantum field theory (QFT) and describe the coupling of a specific charge, e.g. of the electric charge for the electromagnetic force, with a characteristic potential as well as with a thereto linked specific relative strength. An overview on the particles in the SM is given in Figure 1.1. The fourth force, gravitation, could not be formulated in a QFT yet and is not part of the standard model. Its relative strength is so low that it becomes relevant only on the large scale of cosmic objects. For the electromagnetic force the charge, the relative strength and the potential are widely known and well understood, as it frequently appears in daily life. These macroscopic phenomena are described by the Maxwell's equations, while the microscopic aspects are covered by the quantum electrodynamics (QED) which governs the coupling of photons to electric charges. Electrical charges can also be transferred in the weak interaction, via the  $W^\pm$  bosons. Even though these bosons carry an electric charge, the force couples to the weak isospin, an additional quantum number, which is carried by quarks and leptons as well as the gauge bosons  $W^\pm$  and the electrically neutral  $Z$ . It only appears on very short scales because of the high masses of the gauge bosons and its relative strength is small hence it is also called the weak force. On very short scales the dominant mechanism of interaction of quarks and gluons is the strong force, which is formulated in a quantum field theory as quantum chromodynamics (QCD). In this theory all particles which are taking part in the interaction carry a colour charge <sup>1</sup> which is introduced as a SU(3) gauge group. Since leptons do not carry a colour charge, they do not take part in the strong interaction. Of course point-like particles do not appear optically with a visible colour but the behaviour of the charge resembles the properties of the well known additive colour mixing. The interaction is mediated by the eight linearly independent generators of the colour gauge group. These

---

<sup>1</sup>red, green, blue, as well as anti-red, etc.

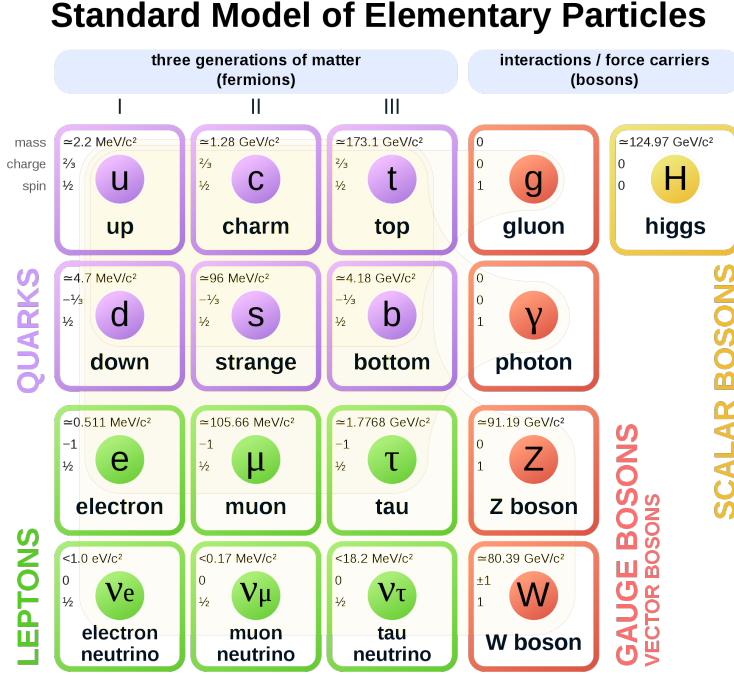


Figure 1.1: Particles of the standard model. Fermions are shown on the left, ordered according to their generations. Bosons are shown on the right. Antiparticles are not shown. [6]

are known as gluons and carry, in contrast to the gauge bosons of the Abelian QED, a combination of colour and anti-colour charge themselves. Gluons thus not only mediate the force but are also able to self-interact which gives rise to the utterly complex behaviour of the strong interaction. The Feynman representations of the possible interactions in QCD are shown in Figure 1.2.

Since no colour-charged particles have been directly observed yet, it is widely accepted that QCD forces partons to be confined to colour neutral<sup>2</sup> states. This is also encoded in the effective potential

$$V(Q^2, r) = -\frac{4\alpha_s(Q^2)}{3r} + kr, \quad (1.1)$$

where  $\alpha_s(Q^2)$  is the coupling constant of the strong interaction depending on the momentum transfer,  $r$  the distance of the interaction,  $k$  a phenomenological constant, which

<sup>2</sup>red, green and blue or colour and the same anti-colour

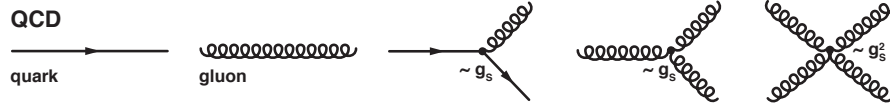


Figure 1.2: *Feynman representations of the basic propagators and vertices in QCD. Every interaction which is possible in QCD can be written as a combination of these basic elements.* [7]

is often called string tension [8]. On small distances the potential acts like a common coulomb attractive potential but on larger distances it changes to a string-like potential where the amount of energy needed to further increase the distance of particles grows monotonically. Eventually a sufficient amount of energy will be stored in the potential to create a new pair of quarks which will then bind to colour neutral hadrons so that no coloured particle will be observed. This process is referred to as string breaking and also plays a crucial role in the Monte Carlo simulation of collider events.

The coupling constant  $\alpha_s$  is also dependent on the momentum transfer and can be calculated in perturbation theory. In first order it is given by

$$\alpha_s(Q^2) = \frac{12\pi}{(33 - 2N_f) \ln(\frac{Q^2}{\Lambda_{QCD}})} \quad (1.2)$$

with  $N_f$  quark flavours and  $\Lambda_{QCD} = 250 \text{ MeV}$  being the scale parameter of QCD [9, 10]. Running coupling results in an asymptotic freedom for large  $Q^2$ , at which quarks and gluons do no longer appear as bound states but rather as free particles. This allows to calculate the matrix elements for interactions perturbatively. On the other hand  $\alpha_s$  diverges for small  $Q^2$  so that around  $Q^2 \approx 1 \text{ GeV}$  perturbation theory breaks down. One approach to overcome these caveats is so called *lattice QCD* where the computed space-time volume is discretised to a grid. Path integrals can then be evaluated following the grid lines and thus divergences are cut. With this technique it is possible to scrutinise phenomena in the domain of low momentum transfers still from the model side which would be inaccessible for a perturbative calculation. [11]

## 1.2 Hot QCD Matter

One additional feature of asymptotic freedom can be deduced when regarding  $\alpha_s$  in dependence of the temperature  $T$  a scale parameter [8]

$$\alpha_s(T) \propto \frac{1}{\ln(T/\Lambda_{\text{QCD}})}. \quad (1.3)$$

This implies the idea of quasi free particles at high temperatures. In this so called QGP the colour charged particles are deconfined and show collective behaviour as their wave functions overlap, similar to the plasma equivalent of atomic matter. Thermodynamical as well as lattice QCD calculations predict a formation of such a state above a critical temperature of  $T_c \approx 150 - 200 \text{ MeV}$  and experimental results do as well given very low net baryon density  $\mu_B$  at  $T_c = (154 \pm 9) \text{ MeV}$  [12]. The exact nature of this phase transition is still unclear but for low  $\mu_B$  no hard phase transition but rather a crossover zone is expected with recent data taken into account [13]. In Figure 1.3 the expected phase diagram is sketched.

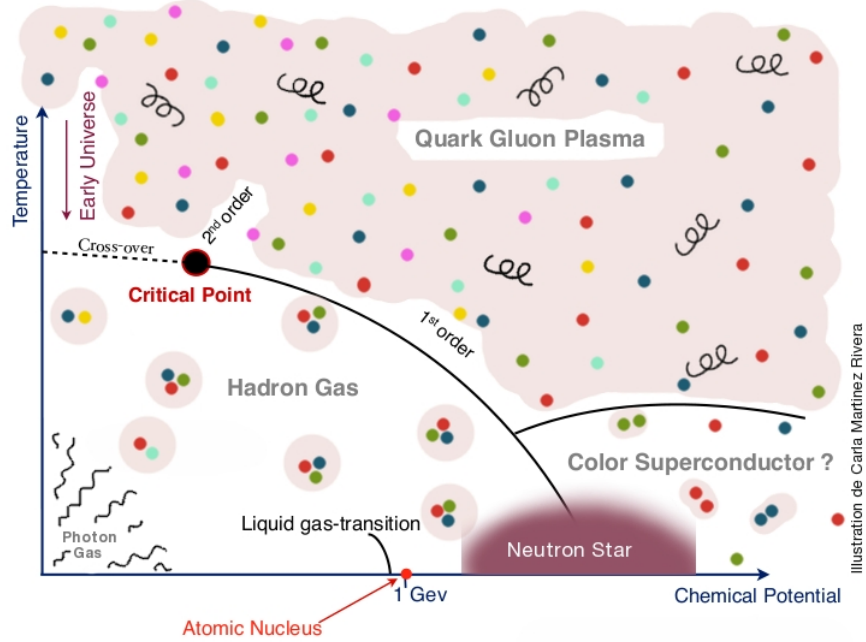


Figure 1.3: Sketch of the phase diagram of hadronic matter. The research at the LHC covers the area to the left with high temperature and low baryochemical potential. The CBM experiment aims for the area where the critical point is expected. [14]



Sufficiently high temperatures are thought to have been reality in the early phases of our universe only  $10^{-6}$  s after the Big Bang [15]. In the further expansion of the universe and the corresponding cooling down the quarks and gluons hadronised to the nuclear matter we still encounter today. Another appearance of a QGP might be in the centre of neutron stars, at large  $\mu_B$  and low temperature. This happens when the Fermi pressure of the neutrons is not strong enough to counter gravitation. The wave functions of the neutrons could then overlap and thus form a state of quasi free quarks and gluons at comparatively low temperatures.

An easier way to observe a QGP in a controlled environment is the use of heavy ion accelerator facilities. In these laboratories one can, depending on the collision system, create different settings of  $T$  and  $\mu_B$  and thereby enable research of different regions of the phase diagram. The ALICE experiment at the Large Hadron Collider (LHC) probes regions of very low  $\mu_B$  at high temperatures where a QGP with a volume unprecedented in laboratory experiments is created. The Compressed Baryonic Matter experiment (CBM) experiment at the new Facility for Antiproton and Ion Research (FAIR) on the other hand will have its focus on high  $\mu_B$  at lower temperatures for the search of a critical point and research on the phase transition at higher baryon densities.

### 1.3 Hard Scattering and Factorisation

In collider experiments two opposing beams of particles are accelerated towards each other such that single pairs of particles might interact. An interaction of two passing particles takes place with a certain occurrence, the so called cross section  $\sigma$ . In classical interpretation a measure for the actual area a particle covers, it can nowadays be more interpreted as probability for the interaction of point like particles [16]. The collision is defined by the centre of mass energy of the particles, here given as the Mandelstam variable  $s$  [17],  $\sqrt{s} = E_1 + E_2$ , mainly the kinetic energy, which then becomes available for particle production. If the system is symmetrical no restraints in the laboratory frame of reference for the scattering angle apply and outgoing particles will be emitted dominantly back to back in a  $2 \rightarrow 2$  process. In collisions of composite particles such as protons or ions, the production of new particles is determined by four main factors. All of them contribute to the measurable observables in the end, but they encode different phases of the collision, which may be separated for, or in theoretical handling via so called factorisation. The final cross section for a certain observable is then given by the product of the evolving processes:

$$\frac{d\sigma}{dO} = \sum_{a,b} \int dx_a x_b \sum_f \int d\Phi_f f_A(x_a, \mu^2) f_B(x_b, \mu^2) \frac{d\sigma_{ab \rightarrow f}}{d\hat{O}} D_f(\hat{O} \rightarrow O, \mu^2), \quad (1.4)$$

where  $f_A$  and  $f_B$  are the parton density functions of the colliding nucleons,  $\frac{d\sigma_{ab \rightarrow f}}{d\hat{O}}$  is the cross section for the given process, and  $D_f(\hat{O} \rightarrow O, \mu^2)$  is the fragmentation function, which governs the evolution of the collision remnants. The integration covers the final state phase space element  $d\Phi_f$  for the observable of interest [18].

These factors will now be described and discussed.

### 1.3.1 Parton Distribution Functions

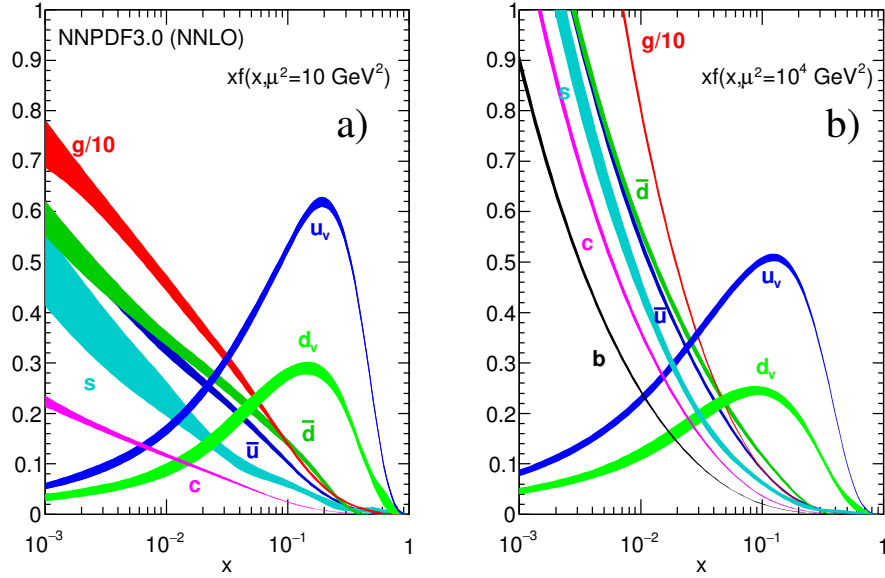


Figure 1.4: Examples of  $x$  times the parton distribution for two different energy scales  $\mu^2$ . It can be seen that for low  $x$  as reached by the LHC gluons are by far the most abundant partons. [19]

For large collision energies, the partonic structure of a hadron is no longer dominated by the valence quarks. Large momentum transfer is equivalent to a high resolution and in the case of QCD this enables resolving the ongoing gluon exchange inside the hadron. Due to the high momenta of the colliding particles and the accordingly short interaction time an incoming parton will see a, by time dilation, frozen snapshot of the partonic substructure of a hadron. Gluon exchange can also be interpreted as radiation of virtual gluons which

again radiate virtual quarks themselves, according to splitting functions  $P$  like

$$P_{q \rightarrow qg}(z) = C_F \frac{1 + (1-z)^2}{z}, \text{ and } P_{g \rightarrow gg}(z) = C_A \frac{1 + z^4 + (1-z)^4}{z(1-z)} \quad (1.5)$$

where  $z$  is the momentum fraction carried by the radiated gluon,  $C_F = 4/3$  and  $C_A = 3$  are the colour factors, which account for the possibilities of colour exchange in this process [18]. Here only the splitting functions for gluon radiation are shown. Other processes can likewise be described in more or less lengthy functions. The radiation itself forms on very low energy scales and is thus non-perturbative. Therefore parton distribution functions (PDFs) are obtained by fits to experimental data e.g. from deep inelastic scattering (DIS) experiments. Examples for one set of PDFs is shown in Figure 1.4. The parton distribution functions can then be scaled to other energies using the Dokshitzer-Gribov-Lipatov-Altarelli-Parisi (DGLAP) equations [19]. An estimate for the probed region of  $x$  is given by [7]

$$x = \frac{2p_T}{\sqrt{s}}. \quad (1.6)$$

### 1.3.2 Cross Section

The hard scattering itself happens in a high momentum transfer regime and can be calculated perturbatively. For this the differential partonic cross section is given by

$$d\hat{\sigma}_{ab \rightarrow f} = \frac{1}{2\hat{s}} |\mathcal{M}_{ab \rightarrow f}|^2 (\Phi_f, \mu, \mu_R) \quad (1.7)$$

The matrix element itself is the sum over the evaluation of all possible Feynman diagrams for the given process. Hitherto Monte Carlo simulations in most cases are limited to tree level diagrams only while some newer approaches also include higher orders to achieve more accurate results [20, 21].

### 1.3.3 Fragmentation Functions

Outgoing partons are far off the mass shell; they are of high virtuality. To move back to the mass shell the partons fragment and thus create real mass in terms of newly generated particles. This process is also governed by the splitting functions already mentioned above but the splittings also appear in a low momentum transfer regime, which is no longer calculable perturbatively. Thus the hadron production in collisions is most commonly described by fragmentation functions (FFs), which essentially give the probability

for a parton to fragment in a certain hadron or set of hadrons:

$$e^+ + e^- \rightarrow h + X. \quad (1.8)$$

These FFs are universal in the framework of factorisation which means that the fragmentation functions measured in the clean environment of  $e^+e^-$  collisions can also be applied to more complex collision systems. Since the FFs only give probabilities they cannot be used in Monte Carlo event generation. The computational models for hadronisation in event generators will be described later in section 3.1.

## 1.4 Heavy Ion Collisions

To investigate the whole phase diagram of hadronic matter it is necessary to create higher energy densities or larger baryochemical potential than possible in collisions of protons. One possibility is to collide heavy ions instead. Since heavy ions are made of protons and neutrons the proceedings of collisions apply to heavy ion collisions quite similarly as to  $pp$  or any other collision system. They also will not interact via their valence quarks but become rather transparent for each other and the interactions happen between the seaquarks and gluons according to the momentum scale of the collision. Yet there are several effects which complicate the understanding of the collisional system. These will be discussed in the following sections.

### 1.4.1 Nuclear Parton Distribution Functions

In nuclei the interplay of the different nucleons enables effects, which change the PDFs in nuclei. A good measure for these effects is the nuclear modification factor [2]

$$R_a^A = \frac{\sigma_{NN}}{\langle N_{bin} \rangle} \frac{d^2 N_{AA}/dp_t d\eta}{d^2 \sigma_{pp}/dp_T d\eta}, \quad (1.9)$$

which gives the ratio of particle yields for different collision systems<sup>3</sup>. Phenomenologically the effects can be described in dependence on the  $x$  they appear at [22]:

- At low  $x < 0.1$  the nuclear parton distribution function (nPDF) is decreased compared to the proton PDF. This effect is called *nuclear shadowing* based on the naive model of an extended nucleus where partons in the front<sup>4</sup> shadow those further back.

---

<sup>3</sup>Here a collision of  $A$  nucleons with  $A$  nucleons is compared to a collision of protons.

<sup>4</sup>In a geometrical picture where front means the direction of movement of the nucleus.

- At  $0.1 < x < 0.3$  an enhancement can be observed, which is called *anti-shadowing*.
- At  $0.3 < x < 0.8$  another depletion was discovered. To date no explanation for this so called *EMC effect* could gain widespread acceptance.
- At  $0.8 < x$  the *Fermi motion* of the partons enables them to carry momentum fractions larger than  $x = 1$ . This effect is more likely in larger nuclei so that it gives rise to another enhancement compared to a proton PDF.

The effects are also shown in Figure 1.5

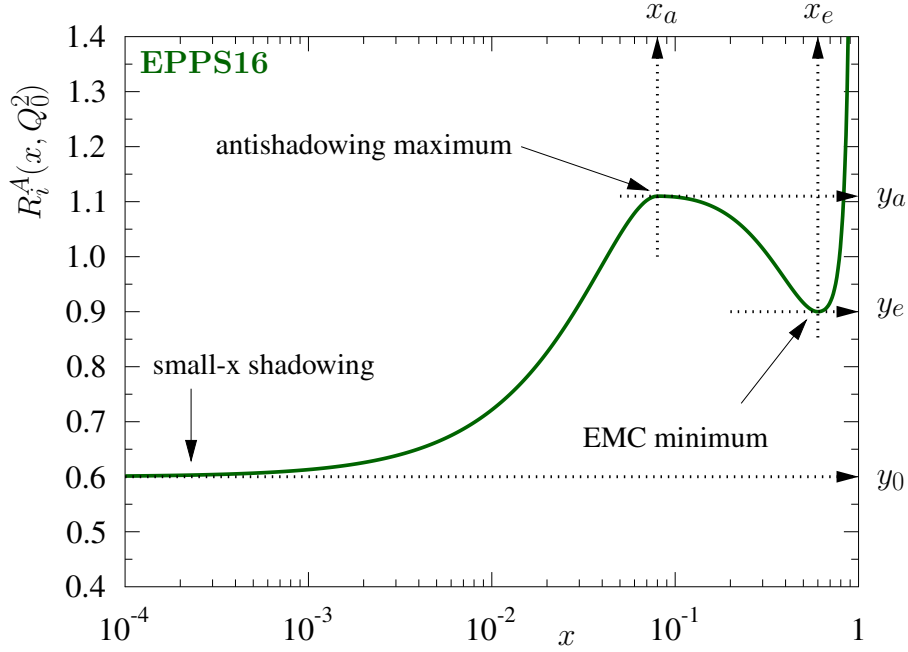


Figure 1.5: Effects on *nPDFs* depending on  $x$ . The nuclear modification factor varies strongly with  $x$ . [22]

### 1.4.2 Collision Geometry

Heavy ions are rather large objects compared to the quantum scale. The more or less spherical nuclei will be Lorentz contracted in their moving direction by a factor of  $1/\gamma$  which makes them appear as flat disks of nuclear matter. These disks will most likely not collide exactly centred so it is necessary to consider the centrality in the collisions. In theoretical descriptions, an impact parameter  $b$ , which controls the number of nucleons that take part in the collision, could be defined. The collision can then be described by the

Glauber model, where the nuclei are described as a composite of colliding nucleons. A sketch of a nucleus-nucleus collision and the determination of participants in the collision is shown in Figure 1.6. With the *thickness functions* for the nuclei

$$T_i(\vec{s}) = \int dz \rho_i(z, \vec{s}), \quad (1.10)$$

where  $\rho$  is the mass number density of the nucleus in dependence of the coordinates in beam direction  $z$  and orthogonally  $\vec{s}$ , and the nucleon-nucleon cross sections  $\sigma_{NN}$ , the number of participants in the collision as well as binary nucleon-nucleon collisions in dependence of the impact parameter  $\vec{b}$  are then given by [8, 23]:

$$N_{\text{part}}(\vec{b}) = \int d^2\vec{s} T_i(\vec{s})(1 - \exp(1 - \sigma_{NN}T_j(\vec{s}))) + \int d^2\vec{s} T_j(\vec{s} - \vec{b})(1 - \exp(-\sigma_{NN}T_i(\vec{s}))) \quad (1.11)$$

$$N_{\text{coll}}(\vec{b}) = \int d^2\vec{s} \sigma_{NN} T_i(\vec{s}) T_j(\vec{s} - \vec{b}) \quad (1.12)$$

Models of this kind are also used for Monte Carlo studies of heavy ion collision.

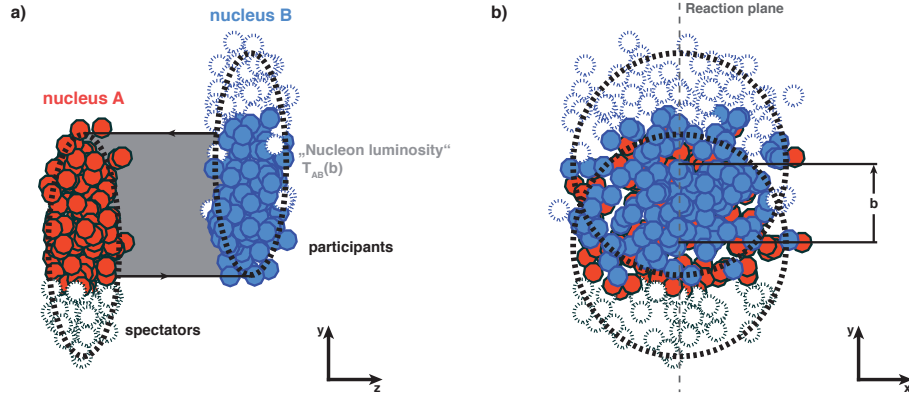


Figure 1.6: Sketch of the collision of two nuclei. The small coloured circles represent nucleons taking part in the collision, the open circles are spectators. This represents the calculation of heavy ion collisions according to the Glauber model. [7]

In experimental studies it is more practical to define the centrality of a collision base on the observed multiplicity of final state particles in the collision, so that e.g. the 5% events with the most final state particles are defined as the 5% most central collisions. The discrimination of the centrality intervals is also shown in Figure 1.7. This approach

can be validated by measuring the non-colliding spectators in the collision. It is also used in a similar way to classify the particle yield in pp or pA collisions.

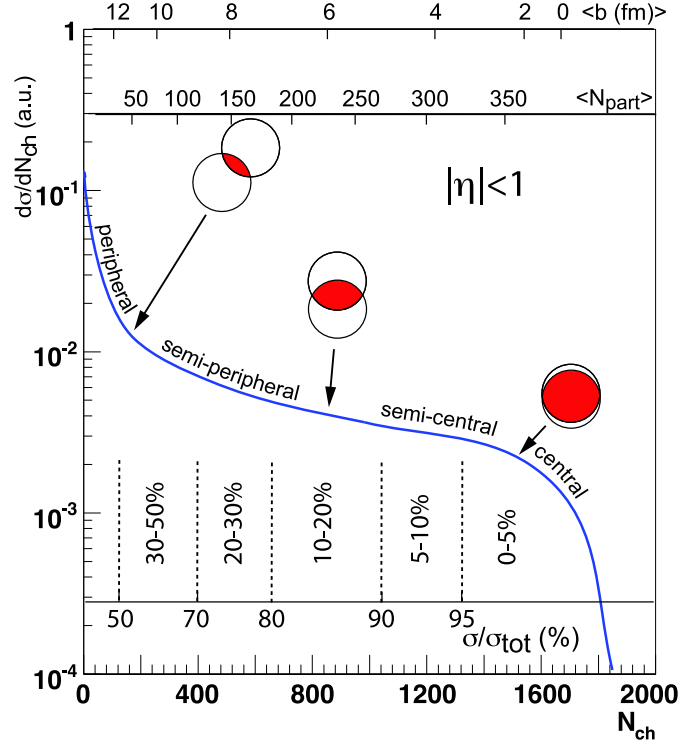


Figure 1.7: *Impact parameters and experimental determination of centrality. The 5% events with the largest multiplicity of charged particles are determined to be the most central events. The centrality classes are determined after the measurements according to the measured multiplicities. [23]*

### 1.4.3 Evolution of the Quark Gluon Plasma

Immediately after the collision the nuclei leave behind a region of heavily excited parton states. These will decay and thermalise until a state of equilibrium is reached after some equilibration time of less than  $\tau_0 \approx 1$  fm.

The expansion of the thermalised QGP can be described with relativistic hydrodynamics. Since the overlap region of the colliding nuclei will most likely not be circular, the QGP acquires asymmetries which gives rise to phenomena of collective flow. Also during the hydrodynamical expansion, the energy density will decrease and the plasma will cool

down. In the following, one expects a *chemical freeze-out* after which the particles species<sup>5</sup> are fixed and after some freeze out time  $\tau_0 \approx 10$  fm the partons finally hadronise to form final state particles. The volume of the QGP is then around  $5000 \text{ fm}^3$  [24]. Figure 1.8 shows a space-time sketch of the subsequent phases of the QGP expanding and cooling down.

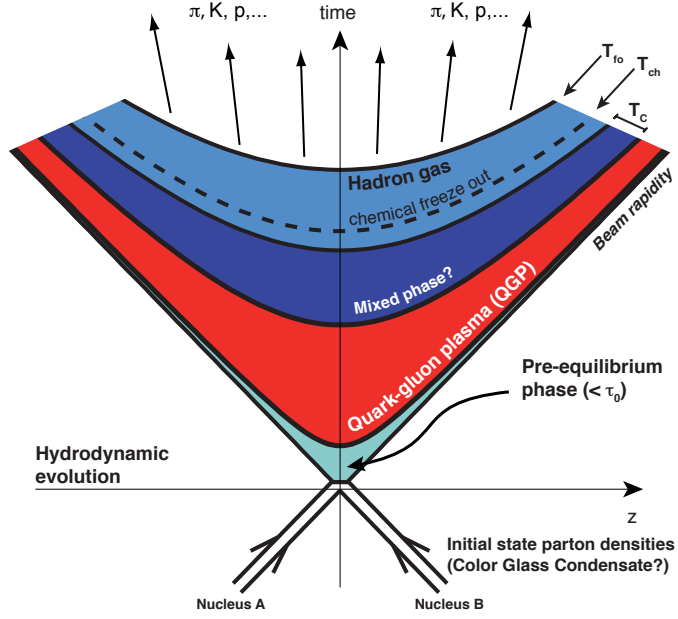


Figure 1.8: Sketch of the space-time evolution of a QGP fireball. The excited medium expands in space with progressing time. Meanwhile it evolves in different phases of cooling down until finally comparably long living particles remain. [7].

<sup>5</sup>quark families etc.



## 1.5 Jet Energy Loss

In heavy ion collisions, the hard scattered particles traverse all the phases of the medium evolution and meanwhile interact with the medium. Experimental results feature these interactions mainly as jet energy loss. This is also a good indication for the occurrence of a QGP as energy loss leads to a jet suppression as observed in jet nuclear modification factor  $R_a^A$ . The interactions can be classified in two main mechanisms, *collisional energy loss* and *radiative energy loss*, which are depicted in Figure 1.9. Both types occur simultaneously but depend on the properties of the medium and the traversing particle. The two mechanisms will be introduced in the following paragraphs and for the relevant case for this thesis a short description of the numerical model will be given.

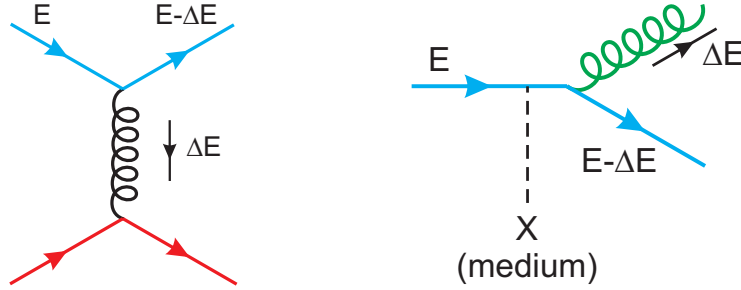


Figure 1.9: Feynman diagrams representing collisional (left) and radiative energy loss (right). A quark with energy  $E$  traverses a medium and loses energy  $\Delta E$ . [18]

### 1.5.1 Collisional Energy Loss

The simplest model for energy loss is the collision of a traversing particle with scattering centres in the medium, where elastic collisions happen statistically. The  $N$  single collisions add up to a total energy loss  $\langle \Delta E_{\text{coll}} \rangle$  so that it is given by the density of scattering centres  $\rho$  and the cross section for a scattering  $\sigma$  times the path length in the medium  $L$  and the average energy loss per scattering  $\Delta E$ :

$$\langle \Delta E \rangle_{\text{coll}} = N \langle \Delta E \rangle = \sigma \rho L \langle \Delta E \rangle \propto L. \quad (1.13)$$

Evaluation of the parameters  $\sigma$  and  $\rho$  needs understanding of the underlying processes. Equation 1.13 finally yields the energy loss per unit length  $dE/dl$  which for light quarks

and gluons is given by:

$$-\frac{dE}{dl}|_{q,g} = \frac{1}{4}C_R\alpha_s(ET)m_D^2 \ln\left(\frac{ET}{m_D^2}\right). \quad (1.14)$$

Where  $C_R$  is the Casimir factor for the effective colour charge, and

$$m_D = 4\pi\alpha_s T^2(1 + n_f/6) \quad (1.15)$$

the Debye mass, the inverse of the screening length, for  $n_f$  active quark flavours [9, 25]. For heavy quarks the energy loss is enhanced by an additional term.

### 1.5.2 Radiative Energy Loss

For light and fast partons the major energy loss mechanism is radiative energy loss, the radiation of gluons along the path through the medium, which can be compared to the well known Bremsstrahlung. On this path the parton acquires momentum or *virtuality* according to the *medium transport parameter*  $\hat{q}$ . The probability of radiating a gluon is then given by the DGLAP splitting functions Equation 1.5, with  $z$  being the radiated momentum fraction, which are modified to account for the medium interactions and the path length through the medium. These changes are often encoded in  $\hat{q} = m_D^2\rho\sigma$ . Logically the total amount of radiative energy loss is therefore path length dependent and given by:

$$\langle\Delta E\rangle_{\text{rad}} \propto \hat{q}L^2 \propto T^3L^2. \quad (1.16)$$

In the case of thin medium where  $L \ll \lambda = 1/\rho\sigma$  the radiated energy is then:

$$\langle\Delta E\rangle \approx \alpha_s\hat{q}L^2 \ln \frac{E}{m_D^2L}. \quad (1.17)$$

In this so called *Bethe-Heitler* regime the path length dependence is reduced by the logarithm. For a thick medium with  $L \gg \lambda$  the cases of soft and hard radiation relative to the characteristic gluon emission  $\omega_c = \hat{q}L^2/2$  have to be regarded. In this *Landau-Pomeranchuk-Migdal (LPM)* regime the total energy loss is then:

$$\langle\Delta E\rangle \approx \alpha_s\hat{q}L^2 \begin{cases} 1 & \text{if } \omega < \omega_c, \\ \ln \frac{E}{\hat{q}L^2} & \text{if } \omega > \omega_c. \end{cases} \quad (1.18)$$

The emission of low energy gluons is suppressed in this regime [7, 8, 18].

### 1.5.3 Higher Twist Energy Loss Model

The thin medium case can be modelled with the so called *higher twist* energy loss model. This model was originally used for the medium modifications in DIS and later adapted for the use in heavy ion collisions. It takes into account terms with higher powers of momentum transfer  $Q^2$  in the splittings, such as multiple scatterings per emission, which are suppressed, while the probability of a splitting is enhanced with medium length  $L$ . The approach is applicable in the regime where factorisation holds as it factors out the initial state and final state parton showers. While the initial state remains unmodified, in the final state the higher twist corrections, additionally more loop Feynman diagrams, which describe the interaction of the parton with the medium, are taken into account. This results in an additional correction to the fragmentation function. The *higher twist* energy loss model is implemented e.g. in a Monte Carlo generator called MATTER [26].



---

## 2 Jets and Observables

As described in the previous chapter, the outgoing partons of a collision will fragment and finally create a collimated spray of particles which is often referred to as a jet. Even though the formation of jets seems quite reasonable to understand, the experimental observable *jet* is not as straight forward. Various additional effects, such as, pileup, initial state radiation (ISR), multiple parton interaction (MPI) or the underlying PbPb-event also create final state particles, which contaminate the clear signal from the hard scattering. This chapter will provide an introduction to the reconstruction of jets as well as some observables that have been defined to gain deeper insights in the underlying physics of jet formation and interaction with a coloured medium.

In the history of particle physics the definitions of jets varied over time and, in particular, for different use cases. The aim to construct a theoretically meaningful yet experimentally robust observable led to the Snomass Accord [27] and finally to the development of the class of generalised  $k_t$ -algorithms [28]. These algorithms aim on clustering according to a certain power  $p$  of the particle  $p_T$  and the radial distance  $\Delta\Phi_{i,j}$  of two particles  $i, j$ . They follow a series of clusterisation steps to (re)construct jets with a certain jet radius parameter  $R$ .

1. Calculate the distance  $d_{ij}$  between all particles as:

$$d_{ij} = \min(p_{T,i}^{2p}, p_{T,j}^{2p}) \frac{\Delta\Phi_{i,j}^2}{R^2}. \quad (2.1)$$

2. Calculate the distance  $d_{i,B}$  between all particles and the beam:

$$d_{i,B} = p_{T,i}^2. \quad (2.2)$$

3. Combine the particles  $i, j$  with the smallest distance to a new pseudojet or if a  $d_{i,B}$  is the smallest distance call this a final jet and remove it from the list.
4. Repeat these steps until all particles are clustered into final jets and removed from the list.

The algorithm is termed differently for the various values which  $p$  can take:  $k_t$  algorithm, if  $p = 1$ , anti- $k_t$  algorithm if  $p = -1$  and Cambridge/Aachen-algorithm if  $p = 0$ . In this thesis extensive use of the latter two is made, because of their clustering properties. While the anti- $k_t$ -algorithm clusters high- $p_T$  particles first and then continues to form rather uniformly circular jets, the C/A algorithm clusters particles with small distances

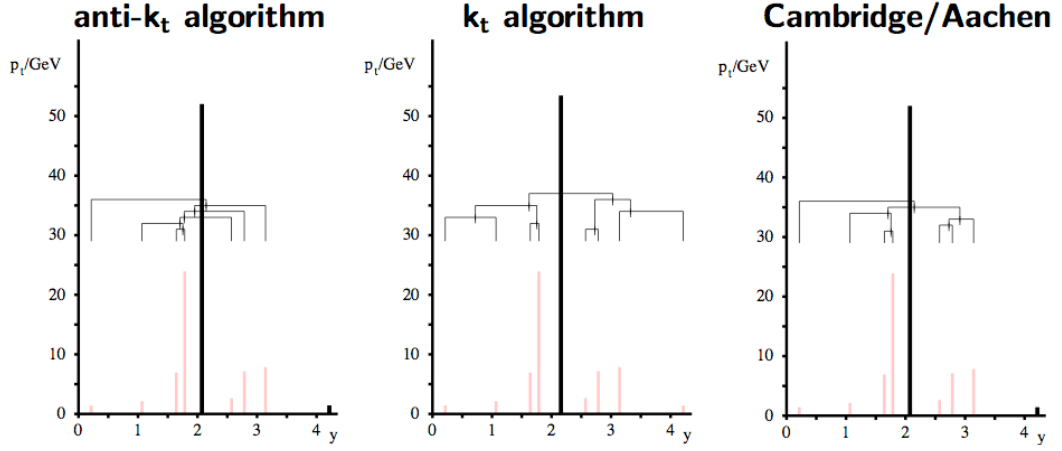


Figure 2.1: The clustering algorithms apply characteristic weighting of angular distance and transverse momentum. The anti- $k_t$  algorithm clusters hard particles first while the  $k_t$  algorithm clusters hard particles last. The Cambridge/Aachen (C/A) algorithm clusters according to radial distance. This results in differences between the algorithms concerning the jets found as well as the clustering history. [29]

first and then continues to combine single prongs to a jet. These strategies help to find the hard jets in a high background environment of a PbPb collision first and then analyse the jet substructure and the splittings, which created high- $p_T$  partons again. Figure 2.1 shows the consecutive construction of jets and the related tree diagrams, which represent the clustering history. In Figure 2.2 the final jets are marked in the  $y - \phi$  plane, where the differences between the clustering algorithms become obvious.

One additional aspect of jet clustering is the recombination scheme, which defines which way the clustered particles should be combined. The standard procedure for all LHC experiments is the  $p_T$ -invariant E scheme, which performs a simple sum of the four-vectors of both particles. For one part of this thesis also the *Winner Takes it All* recombination scheme is used. This recombination scheme adds the transverse momentum of the recombined particles and the result obtains the rapidity and azimuth of the harder particle. In this procedure the mass of the jet is the mass of the higher- $p_T$  particle. Softer particles do not contribute to the jet mass. Thus the jet is centred towards the hardest particle and the analysis is more sensitive to deflection of the outgoing parton but less sensitive to wide angle radiation in the fragmentation.

The most commonly used software for jet finding is called *FastJet* [30] and was developed by Matteo Cacciari, Gavin Salam and Gregory Soyez. FastJet has optimised the algorithms for generalised  $k_t$  jet finding, scaling only with  $N \ln N$  for  $N$  particles, compared to the naive implementation, which scales with  $N^3$ . Hence it is called fast. Furthermore the

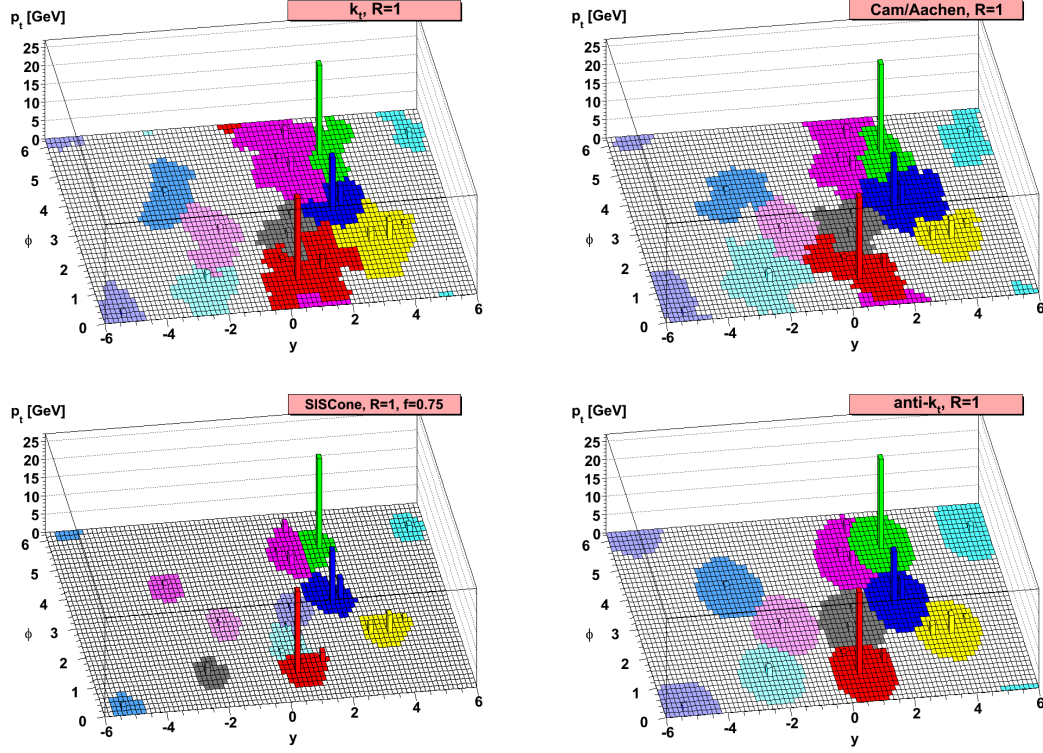


Figure 2.2: Clustered jets in the  $y - \phi$  event plane. The different clustering algorithms yield different kinds of jets concerning shape of the final jet and distribution of the jets. Also characteristics such as the jet area vary with different algorithms. [28]

framework provides classes for handling jets and all clustered constituents of the jets and has internal routines for background handling as well as an open API for user contributions which can be distributed with the *fjcontrib* package. The terminology for the description of jets in this thesis is consistent with the corresponding objects in the FastJet framework.

For a further analysis of jets the internal structure of the clustered jets is an interesting objective. To learn more about QCD and jet physics numerous observables have been created. The ones used in this thesis will be presented and discussed in the following sections.

## 2.1 Substructure Observables

To analyse the internal structure of jets one can define observables, which measure how evenly the  $p_T$  is distributed amongst the jets constituents and inside the jet cone. In this thesis two observables are investigated called the momentum dispersion:

$$p_TD = \frac{\sqrt{\sum_i p_{T,i}^2}}{\sum_i p_{T,i}} \quad (2.3)$$

and the radial moment:

$$g = \sum_{i \in jet} \frac{p_T^i}{p_{T,jet}} |\Delta R_{i,jet}|, \quad (2.4)$$

using the same notation as above. Both observables have a range of possible values between 0 and 1. Momentum dispersion measures the distribution of  $p_T$  amongst the jet particles in a way that jets with many low energetic constituents exhibit low  $p_TD$  conversely jets with few high energetic constituents exhibit high  $p_TD$ . The radial moment is complementary in the sense that narrowly collimated jets have small radial moments and wider jets have larger. Thus one expects jets in a QGP to have lower  $p_TD$  and larger  $g$  than their correspondents in vacuum. This can be seen in the plots in Figure 2.3 which are taken from [31]. The same phenomena apply to gluon jets, which fragment to a greater number of less energetic particles, which are more evenly spread in the jet cone than quark jets.

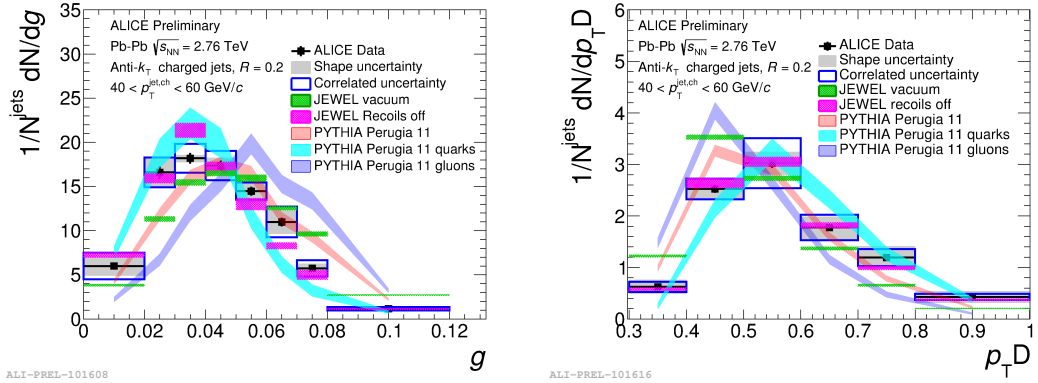


Figure 2.3: Jetshapes  $g$  (left) and  $p_TD$  (right) as measured with the ALICE experiment in comparison with different Monte Carlo generators as well as quark and gluon jets. Note that the gluon jets tend to smaller  $g$  and larger  $p_TD$  and vice versa for the quark jets, compared to data and unselected event generation.[31]



## 2.2 The Lund Jet Plane

The phase space of the splittings inside a jet is represented in so called *Lund diagrams* [32], which plot  $\ln k_t$ , against  $\ln 1/\Delta$  for each jet splitting. The variable  $k_t$  denotes the momentum which the radiated gluon acquires transversely to direction of movement of the original parton and  $\Delta$  denotes the radial distance of the splitting. Apart from theoretical calculations, these properties can also be reconstructed in experimentally observed jets. For this purpose jets are declustered utilising the following algorithm:

1. Cluster the event with a jet finding algorithm of choice (Usually today anti- $k_t$ -algorithm is used).
2. Recluster each single jet with the C/A-algorithm.
3. Undo the last step of clustering to obtain two subjets  $j_a$  and  $j_b$  with  $p_{t,a} > p_{t,b}$  so that  $j_b$  is an emission.
4. Calculate the splitting variables:

$$\ln(k_t) = \ln(p_{t,b} \cdot \Delta R_{ab}) \text{ and } \ln(1/\Delta) = \ln(1/\Delta R_{ab}). \quad (2.5)$$

5. Repeat from 3. for  $j_a$  until  $j_a$  is a single constituent.

One of the advantages of the 2D representation is the physically robust identification of different physics properties of the splittings. On the one hand different formation times of the splittings can be represented in the diagram, as well as combinatorial background, hard- and soft-splitting regions can be identified on the other hand. It is important to note that the construction of the *Lund plane* is not infrared and collinear (IRC)-safe since every splitting is added as one entry point. Depending on the clustering a splitting of a soft radiation can therefore either be declustered as an entry to the diagram or can be summed up in a larger declustered branch. Yet thanks to the fact that the regions in the *Lund plane* are well defined these soft emissions appear in their own region so that other regions are practically free of soft emissions. That makes isolated regions in the diagram IRC-safe again. This allows for technically simple yet physically meaningful geometrical cuts on Lund Plane Diagrams to isolate certain regions of interest so that *Lund diagrams* offer a great way to compare calculations and Monte Carlo generators with experimental data [32].

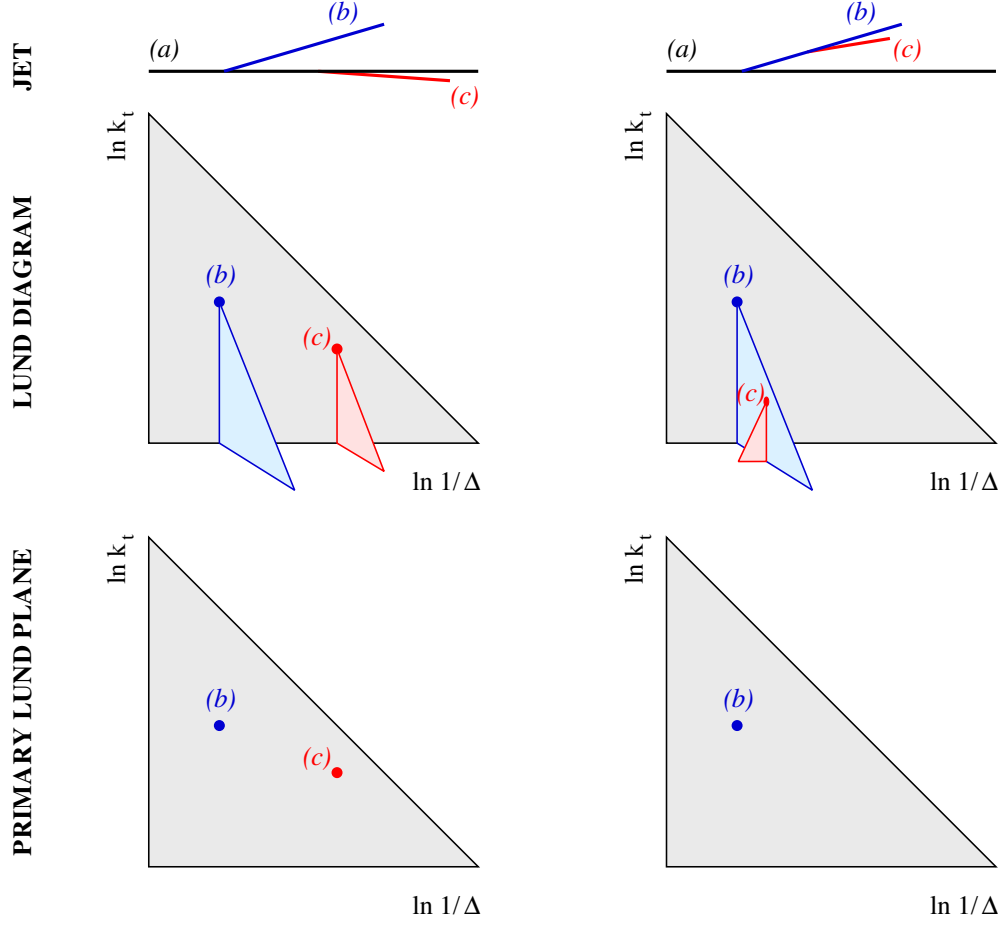


Figure 2.4: Construction of the Lund plane for two different follow ups of splittings. On the left the two splittings from the hardest parton (black) end up in the Lund plane, while on the right only the first splitting is taken to account. Additionally it would be possible to create a secondary Lund plane (mid right) which could show the splitting of the radiated particle. [32]

For a more quantified analysis the density

$$\rho_{\text{Lund}}(\Delta R, k_t) = \frac{1}{N_{\text{jet}}} \frac{dn_{\text{emission}}}{d \ln k_t d \ln 1/\Delta R} \quad (2.6)$$

is proposed. Figure 2.4 shows the construction of the *Lund planes* for two different jets where one can see how only the splittings of the hardest branch are regarded for the *Lund plane*. In Figure 2.5 it is shown how splittings with different properties are represented in the different regions in the *Lund plane*.

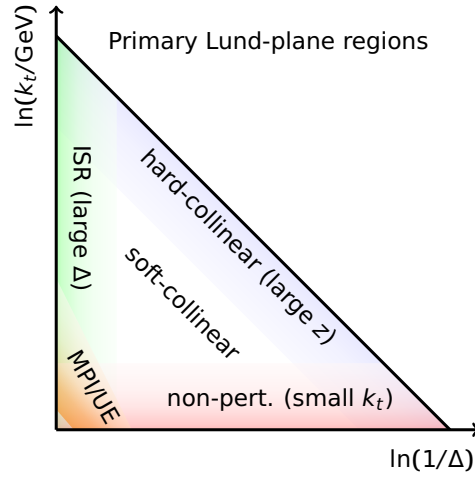


Figure 2.5: Sketch where different properties of splittings can be found in a lund plane [32]

In the recent years machine learning (ML) techniques started to gain increasing importance in analysis approaches due to their improved discrimination power, e.g. for certain heavy particle jets, over manually constructed observables and despite the caveat of limited insight in which properties actually cause this increased discrimination. *Lund plane* analyses can provide a link between the established approach and the new machine learning methods making use of the theoretically well definedness as described above. The ML analysis of a *Lund plane* can even ‘yield superior performance as compared to jet images’ [32] and thus could lead to a better understanding of the ML. It is also reasonable to further analyse the discarded branches in *lund planes* of higher order as in the right panel in Figure 2.4. Even though these kinds of representations are no longer intuitive for human visual understanding they can provide input for machine learning driven analysis.

### 2.3 Soft Drop

For many physics cases it is considered useful to identify the initial splittings during the jet formation. One approach is the so called Soft Drop declustering [33], which was developed by Larkoski et al. and is distributed in *fjcontrib*. Soft Drop makes use of the angular ordering of the C/A jet algorithm, in which particles with small angular distance are clustered first. The workflow of Soft Drop declustering is then as follows:

1. Cluster the event with the jet finding algorithm of choice (Usually today anti- $k_t$ -algorithm is used).
2. Recluster each single jet with the C/A-algorithm.
3. Undo the last step of clustering and check whether the condition:

$$z_g = \frac{\min(p_{T,1}, p_{T,2})}{p_{T,1} + p_{T,2}} > z_{\text{cut}} \Theta^\beta, \quad (2.7)$$

is fulfilled.

4. Repeat from 3. until it is fulfilled. This jet is now either tagged or will be treated as groomed, depending on the mode Soft Drop is running at.

It is important to consider the influence of the parameter  $\beta$ . If  $\beta < 0$  Soft Drop will return jets with exactly two hard prongs and thus acts as a tagger for decays of heavy particles such as t-quarks. If  $\beta \geq 0$  Soft Drop grooms the jet and removes all soft and wide angle radiation which does not fulfil the Soft Drop condition Equation 2.7. With this setting Soft Drop can also be used to remove pileup or QGP background from jets.

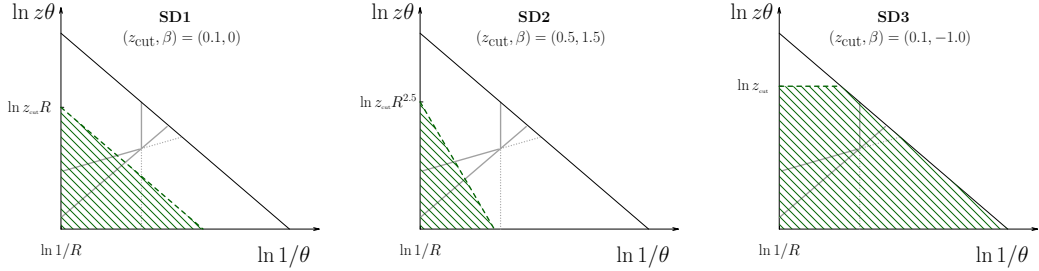


Figure 2.6: Soft Drop grooming area in the Lund plane. The shaded area is groomed. [34]

Soft Drop is well defined from a theoretical point of view, meaning it can be calculated perturbatively without complications due to infrared collinear or ultraviolet divergencies.

Furthermore Soft Drop grooms well defined regions in the Lund Plane which can be set with the Soft Drop parameters  $\beta$  and  $z_{cut}$ . This is also shown in Figure 2.6.

## 2.4 Recursive Soft Drop

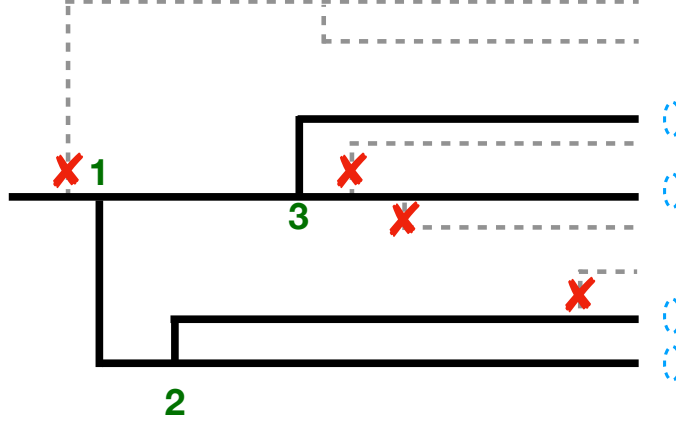


Figure 2.7: *Recursive Soft Drop successively removes soft constituents from the jet. This schematic drawing shows the order of declustering. All grey dashed lines are groomed for  $N > 3$ . The blue circles would then remain as the final jet. [32]*

Most likely there is not only one hard splitting in a jet but rather a cascade of splittings with large momentum transfer, additional to pileup from other collisions or heavy ion background. Recursive Soft Drop accounts for this by looking for a number of splittings  $N$  to fulfil the Soft Drop condition, finally receiving  $N + 1$  branches using the following procedure:

1. Set the list of branches to the single initial C/A reclustered jet.
2. Split the branch with the farthest apart parents in  $\Delta R$  to  $j_1$  and  $j_2$ . Remove that branch from the list.
3. Test whether the branches pass the Soft Drop Condition. If so, add both, if not add only the harder to the list of branches.
4. Repeat from step 2.

Figure 2.7 shows a graphical representation of this grooming procedure. Obviously  $N = 0$  returns the original ungroomed jet and  $N = 1$  corresponds to the original Soft Drop. A more detailed description of the properties of recursive Soft Drop is given in [32].

## 2.5 Recoil Jets

Since the dominant types of hard scatterings are  $2 \rightarrow 2$  processes, angular correlations in angular jet distributions can be meaningful observables to investigate effects of jet medium interactions [35]. In this thesis hadron jet correlations, the distribution of jets recoiling from a single hard hadron trigger, are investigated.

### 2.5.1 Recoil Jet Definition

Recoiling jets in this investigation are jets in a region covering  $\pi - 0.6 < \varphi \leq \pi$  with respect to the trigger hadron. Inside this region all jets are taken to account:

$$\frac{1}{N_{\text{trig}}^{\text{AA}}} \frac{d^2 N_{\text{jet}}^{\text{AA}}}{dp_{T,\text{jet}}^{\text{ch}} d\eta_{\text{jet}}} \bigg|_{p_{T,\text{trig}} \in \text{TT}} = \left( \frac{1}{\sigma^{\text{AA} \rightarrow \text{h} + \text{jet} + \text{X}}} \cdot \frac{d^2 \sigma^{\text{AA} \rightarrow \text{h} + \text{jet} + \text{X}}}{dp_{T,\text{jet}}^{\text{ch}} d\eta_{\text{jet}}} \right) \bigg|_{p_{T,\text{h}} \in \text{TT}} \quad (2.8)$$

The spectra are corrected for background by subtracting the average background density in the event from the jet  $p_T$ . For pp events the background density  $\rho$  is determined by calculating the amount of transverse momentum inside two cones orthogonal to the trigger hadron in  $\varphi$  and at the same  $\eta$ . In PbPb events the jet-median background estimator provided with the FastJet framework is used, which gives  $\rho = \text{median}\{p_{T,\text{jet}}^{\text{raw},i}/A_{\text{jet}}^i\}$ . Therefore the reconstructed  $p_{T,\text{jet}}^{\text{reco},i}$  can be written as:

$$p_{T,\text{jet}}^{\text{reco},i} = p_{T,\text{jet}}^{\text{raw},i} - \rho \cdot A_{\text{jet}}^i, \quad (2.9)$$

where  $p_{T,\text{jet}}^{\text{raw},i}$  and  $A_{\text{jet}}^i$  are given for every jet  $i$  in the acceptance area and  $\rho$  is calculated for the event. This results in the jets with less than median  $p_T$  to contribute to the spectrum with negative values, which will later be used for normalisation. For the calculation of the observables two different classes of trigger hadrons are used. One reference class with trigger hadrons ranging from 8 GeV to 9 GeV and one signal class with a range from 20 GeV to 50 GeV. The events are randomly assigned to either the reference or the signal trigger class, such that half of the events are analysed for the reference class and the other class for the signal class. Previous measurements have shown an excess for the signal trigger class in higher  $p_T$  [35].

### 2.5.2 Recoil Observables

The excess in larger  $p_T$  is measured as  $\Delta_{recoil}$  according to

$$\Delta_{recoil} = \frac{1}{N_{trig}^{AA}} \frac{d^2 N_{jet}^{AA}}{dp_{T,jet}^{ch} d\eta_{jet}} \Big|_{p_T, trig \in TT_{Sig}} - c_{Ref} \cdot \frac{1}{N_{trig}^{AA}} \frac{d^2 N_{jet}^{AA}}{dp_{T,jet}^{ch} d\eta_{jet}} \Big|_{p_T, trig \in TT_{Ref}}. \quad (2.10)$$

The correction factor  $c_{ref}$  is determined by a linear fit to the ratio *signal/trigger* in the region around  $p_T \approx 0$ . A similar procedure can be applied to measure the angular distribution of the recoil jets.

$$\Phi(\Delta\varphi) = \frac{1}{N_{trig}^{AA}} \frac{d^2 N_{jet}}{dp_{T,jet}^{ch} d\Delta\varphi} \Big|_{p_T, trig \in TT_{Sig}} - c_{Ref} \cdot \frac{1}{N_{trig}^{AA}} \frac{d^2 N_{jet}^{AA}}{dp_{T,jet}^{ch} d\Delta\varphi} \Big|_{p_T, trig \in TT_{Ref}} \quad (2.11)$$

This can hold as a measure for the deflection of jets in the QGP and is quantified via

$$\Sigma(\Delta\varphi_{thresh}) = \int_{\pi/2}^{\pi - \varphi_{thresh}} d\Delta\varphi [\Phi(\Delta\varphi)]. \quad (2.12)$$

These observables will be analysed with two different jet recombination schemes, namely the default *E-scheme* which weighs the jet axis according to the transverse momentum of the constituents and the *Winner-takes-it-all-scheme* where the transverse momentum of all constituents is added to the constituent with largest  $p_T$ . This can cause a slight shift of the jet axis respectively and thus change  $\Phi(\Delta\varphi)$  and  $\Sigma$ . The aim is to evaluate the sensitivity of the recombination scheme to scatterings in the QGP.





---

## 3 Computational Methods for Jet Observable Analyses

For the development and evaluation as well as for reference purpose it is often helpful to use so called event generators. As described above, while possible to analytically calculate spectra for several observables in high energy particle physics, many aspects of hadron collisions are beyond the scope of perturbative quantum field theories. Monte Carlo simulations can overcome this apparent obstacle by sampling probabilities of the possible outcomes of collisions and by therefore generating certain aspects or even full events according to theoretical considerations. Typically a tuning to experimental data is performed. In the history of accelerator experiments many different Monte Carlo event generators have been and are still being developed. In this thesis two different software packages are used, the well established PYTHIA [4] event generator and the very recently developed JETSCAPE [5] framework. Additionally some aspects of collisions, e.g. thermal background, can be simulated with rather simple toy models. Finally multiple analysis routines have been implemented as a part of the work for this thesis.

### 3.1 PYTHIA 8.2

PYTHIA is a multi purpose event generator for the simulation of lepton and hadron, e.g. proton, collisions with  $\sqrt{s} > 10$  GeV, where nuclear resonances have no significant contribution. Its long history of development reaches from Large Electron-Positron collider (LEP) experiments up to the present where PYTHIA is one of the most commonly used Monte Carlo generators in LHC experiments. The events are created in vacuum and no interaction with matter is included. For full detector simulations further programs such as GEANT [36] are required. Nonetheless studies with PYTHIA alone can give good insights in the feasibility of measurements as well as a well established reference to unfolded and corrected measurements. Events in PYTHIA are generated in the factorised approach described in [4].

The hardest process is described with matrix elements of leading order accuracy. The input for the hard process is given by PDFs of which PYTHIA has several sets included. These  $2 \rightarrow 2$  but also  $2 \rightarrow 1$  and  $2 \rightarrow 3$  processes are calculated by the process level class. In this thesis only the QCD processes are used.

Additionally ISR and the hard fragmentation are handled by parton shower algorithms which are based on the splitting functions. Starting from the hard process the parton

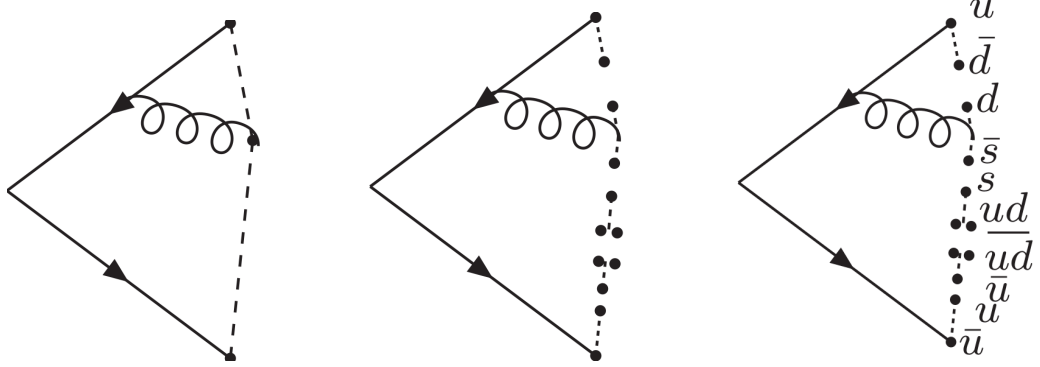


Figure 3.1: Sketch of the Lund string model of hadronisation. From left to right the strings break and form hadron from quarks. [37]

shower is represented as time-like evolution forward in time while the ISR is considered a space-like shower, which evolves backwards in time. These are generated by the parton level class. These routines have an accuracy of leading logarithmic order.

In hadron-hadron collisions MPI can occur and contribute to the overall event activity. Since the event is being constructed around the hardest collision MPI can be considered as underlying event.

After the perturbative parton showering reaches the lower limit for radiation the generated partons need to be combined into colour neutral hadrons. This process is handled by the so called string fragmentation model where the single partons are connected with colour strings. According to the linear term of the QCD potential the strings are given a tension of  $\kappa \approx 1 \text{ GeV fm}^{-1}$ . As the partons move apart the energy stored in the string increases until eventually there is sufficient energy stored for the creation of an additional pair of quark and anti-quark. This process is also depicted in Figure 3.1. This idea resembles the observed confinement and is supported by lattice QCD models. Due to the gradual nature of this process, the energy increases linearly with distance, the creation of lighter quarks is enhanced compared to heavier ones. For higher energetic particles the string breaking continues until all the particles have reached the mass shell and thus become final state hadrons.

### 3.2 The JETSCAPE Framework

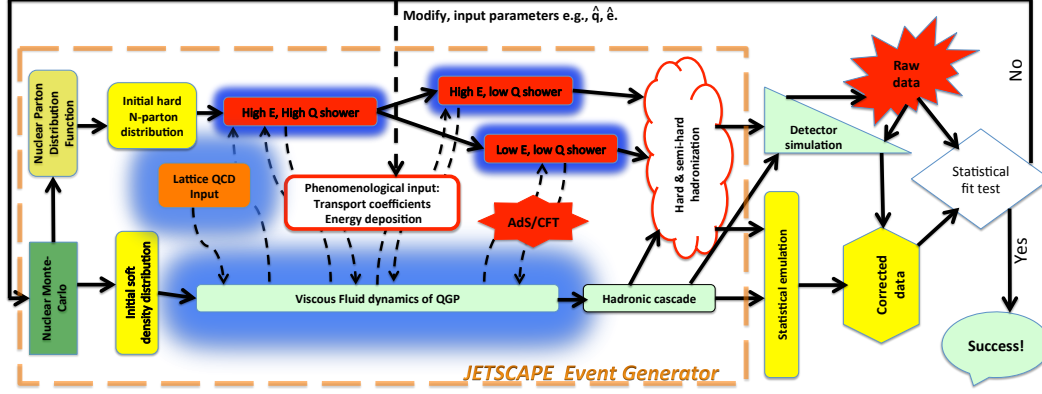


Figure 3.2: Schematic representation of the program flow in JETSCAPE. [5]

The JETSCAPE Framework was designed to support Bayesian analysis of multiple physics cases in the evolution of jets in a QGP. For the sake of comparability of the wide range of different approaches to the formation and evolution of heavy ion collisions JETSCAPE provides a framework for the Monte Carlo generation of those events as well as implementations for the most common theoretical models of jet energy loss and medium modifications. JETSCAPE covers the different stages of the collision in a factorisation-like approach where the various physics effects are calculated independently from each other. For every stage of the collision the user can choose from different modules with varying physics cases for the use in the analysis. The different stages are shown in Figure 3.2 and will shortly be described.

- The *Initial State* or nuclear Monte Carlo is set up with TRENTO [38], a model, which calculates the initial conditions in nuclear collisions. For the determination of the single scattering centers inside the nuclei a Glauber Monte Carlo is used. Furthermore the initial entropy density of the collision, which is a measure for the energy stored in the passing through of the nuclei, is determined. For JETSCAPE there are several predefined settings for AuAu and PbPb collision systems at the energies of the RHIC and LHC. The output is the spatial distribution of vertices for the individual nucleon-nucleon collisions as well as the entropy density at  $\tau_0$ .
- A *pre-hydrodynamics* module propagates the entropy density up to some switching time  $\tau_s$  where the medium can be described by viscous hydrodynamics.
- The evolution of the medium is described by *relativistic hydrodynamics* for which JETSCAPE offers multiple options of programs such as MUSIC. These programs

solve the relativistic hydrodynamics equation to calculate the time evolution of the medium until hadronisation sets in. In this module the transport coefficient  $\hat{q}$  is the most important parameter to adjust.

- For the initiation of jets JETSCAPE provides two routines to create highly energetic *hard partons* in the collision. The first is the rather simple parton gun, which fires partons at a fixed momentum through a cuboid bulk of QCD medium called a brick. These partons will (in the current generation of code) always be  $u$ -quarks. Studies on other partons therefore require a more sophisticated generator, which is provided by the PYTHIA Monte Carlo event generator. JETSCAPE includes PYTHIA so it is possible to use the whole functionality of the event setup including process selection and  $\hat{p}_T$ -range of the collision. After the generation of outgoing partons the handling is again taken over by JETSCAPE where the partons are propagated through the medium according to the hydrodynamics simulation as well as the energy loss.
- JETSCAPE comes with several *energy loss* modules for a wide range of energy loss formalisms. In the standard procedure down to a predefined value of the virtuality of a parton  $Q_0^2$  the medium interactions are handled by the MATTER [26] implementation of the *higher twist* mechanism, which generates a medium modified virtuality ordered parton shower. For lower virtuality there are more options such as LBT, MARTINI or AdS/CFT. These will handle elastic as well as inelastic scattering according to somewhat different implementations which are described in more detail in [5]. In general the user is free to compose different workflows for the simulations. It is possible to choose from different shower handling procedures including the original PYTHIA shower as well as MATTER shower generation, which also ensures a smooth transition from the medium into the vacuum. This method is also used in this thesis.
- *Hadronisation* is, again, carried out by the PYTHIA implementation of the Lund string model. For this model the user can choose from *coloured hadronisation* and *colourless hadronisation*. In the coloured case the colour charge of each parton is tracked during the whole sequence of the parton shower generation, especially if it is done by PYTHIA. For the use of MATTER or the other energy loss modules for the final state of the parton shower this cannot be done as they do not track colour charge. In fact for a parton shower inside a QGP medium it can be assumed that colour is permanently exchanged and thus tracking is not necessary. After the shower in the energy module has finished string connections according to the Lund string model are established, while making sure no colour charge remains unpaired. The strings are set between quarks with the lowest radial distance to create the shortest possible strings, and finally the gluons are assigned to the again closest possible strings and the event is passed to PYTHIA for the final hadronisation.

- After the plasma is cooled, relativistic hydrodynamics is no longer the proper framework to describe the fireball but a *hadronic afterburner* can be added to simulate the hadronic decays and scatterings.

### 3.3 Background Toy Model

Since the JETSCAPE framework only provides the modules for the hard scattering and the medium modifications for traversing particles, an additional module was needed to fill the generated events with combinatorial QCD background. In this thesis a simple toy model was used for this task. The basic functionality of this toy model is to get random particle tracks and multiplicities from a dataset of heavy ion collisions. The random tracks will then be identified as charged pions with an extra identifier, which tags the particles as background. The particles are then filled to the list of FastJet pseudojets. This step is repeated until the randomly drawn multiplicity is reached. This approach allows to create individual background for each event, which is still distributed according to the real measured distributions. Still it does not account for more complex yet basic effects like collective flow.

### 3.4 Analysis Tools

For each part of the investigations special analysis code is implemented. For the jetshape and recoil jet analysis events are created on the fly with PYTHIA and then immediately analysed. This procedure limits the amount of storage space needed without negative effects on the performance. The analysis tasks are the more computing time consuming parts of the programmes, especially for the recoil jet analysis, where the same event is analysed several times with different settings for jet radius and recombination scheme. Therefore this analysis is carried out in several  $\hat{p}_t$  bins.

The workflow for JETSCAPE analyses separates the generation and analysis of the events. In a first step the events are generated according to the settings, which can be supplied in an .XML file. For a faster generation the hydrodynamics calculations can be reused for several events and  $\hat{p}_T$  bins can be set to enhance statistics for jets with large transverse momenta. The events are finally written to files. The second step is to load these events using the JETSCAPE *reader* class and feed them to FastJet analysis routines. In this thesis the *Lund diagrams* are generated using the Lund routines, which are provided in the *fjcontrib* package. An API for Python programming is also provided.



---

## 4 Evaluation of Analysis Routines

In this chapter, simulations for the analysis techniques as described in chapter 2 will be presented and discussed. First some insights to the impact of Recursive Soft Drop on jets from heavy ion collisions are given. In this point the analysis focuses on the question whether RSD can be a tool to reduce background contributions to a variety of physics observables. The second part is the evaluation of a recoil jet analysis with special focus on the jet recombination scheme. Several aspects of hadron jet correlations are investigated with respect to the sensitivity on large angle scattering. The analysis follows [35] but compares two recombination schemes and the large angle splittings of quark-jets and gluon-jets. The third part gives a brief view on analyses in the Lund jet plane with JETSCAPE and combinatorial background. Since JETSCAPE is a comparably new event generation framework the workflow and the possibilities are discussed with the example of the *Lund plane* density. The analyses are conducted with a separate analysis script each so that the settings and statistics differ. Thus they should be regarded as independent studies, each on its own topic, in the frame of an explorative thesis. Nonetheless the kinematic settings stay the same for all tasks. They are set to match the capabilities of the ALICE experiment for jet analyses. Accordingly the jets are reconstructed from charged particles with a maximum rapidity  $\eta < 0.9$  and a minimum transverse momentum of  $p_{T, \min} > 0.15$  GeV. Furthermore the centre of mass (CMS) energy of all collisions is set to  $\sqrt{s} = 2.76$  TeV.

### 4.1 Background Reduction for Jetshape Observables

The impact of RSD on jets in events, which have been created with PYTHIA and are embedded in additional background is investigated in this part of the thesis. The data sample contains 10 million events, which are created with PYTHIA using the `HardQCD:All`<sup>1</sup> setting with a minimum  $\hat{p}_{T, \min} = 10$  GeV. Since a minimum  $p_T \geq 40$  GeV is required for the reconstructed jets, lower  $\hat{p}_T$  and the `SoftQCD` regime can be neglected here. For this analysis RSD is applied with a depth ranging from no Soft Drop up to ten recursions where for each depth of recursion the distributions for all observables are stored. Accordingly the shown distributions are the result of applying RSD with depth  $n$ . As an example Figure 4.1 shows the  $p_T$  distribution of all jets after  $n$  recursions of RSD. It is clearly visible that the distribution is shifted towards lower  $p_T$  by application of the Soft Drop. This effect also emerges with the recursive application, for which after few steps the high  $p_T$

---

<sup>1</sup>HardQCD is the regime, in which PYTHIA generates events according to perturbative QCD

region undergoes only slight changes. Moreover the region  $p_{T,\text{jet}} \leq 50 \text{ GeV}$  is enhanced and the plateau created by the combinatorial background is progressively removed.

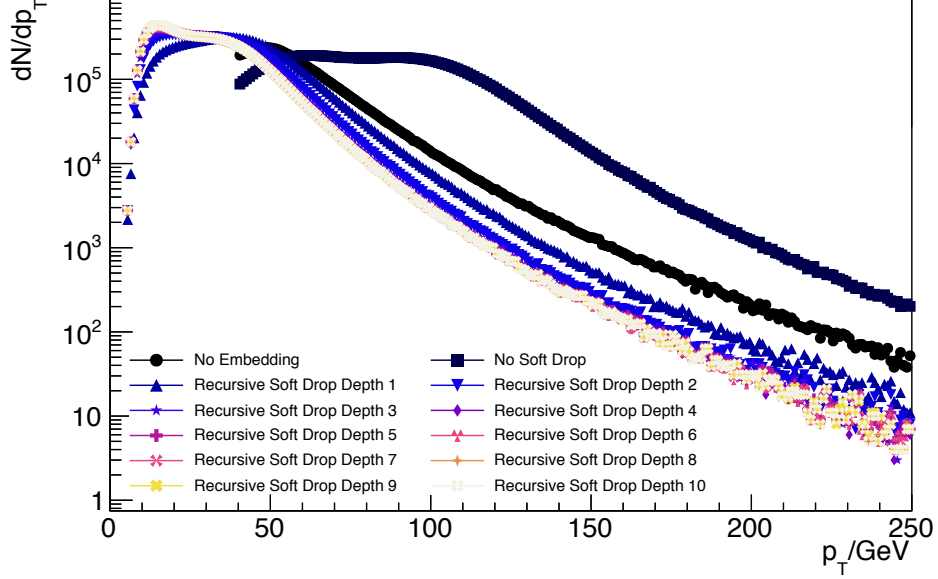


Figure 4.1:  $p_T$  of the reconstructed jets after  $n$  recursions of Soft Drop.

In Figure 4.2 the distributions of additional observables are shown. The most qualitative changes are observed for the first recursion of RSD while the continuing grooming shows the same behaviour as already observed for the distribution of  $p_{T,\text{jet}}$ . As expected the number of background particles removed from the jet increases while the number of background particles in the jet decreases. Regarding the jet momentum dispersion and radial momentum one can clearly see the qualitative change after the first recursion of RSD while the further recursions even still enhance this effect. As described in section 2.1 the jetshapes are a measure for the evenness of the fragmentation and thus whether a jet is more likely a quark or more likely a gluon jet. In the plot for  $p_t D$  and  $g$  one can see that embedded events in general appear more gluon like when regarding the jet shapes, as was also observed in [35]. Yet when RSD is applied this behaviour is changed to a more complex picture, in which the existence of quark as well as gluon jets is also visible in the distribution. This can also be interpreted as the qualitative response of the jetshape to background removal.

For a more quantitative analysis, for all observables moments of the distributions are plotted. In Figure 4.3 the mean value, the most probable value as well as the standard de-



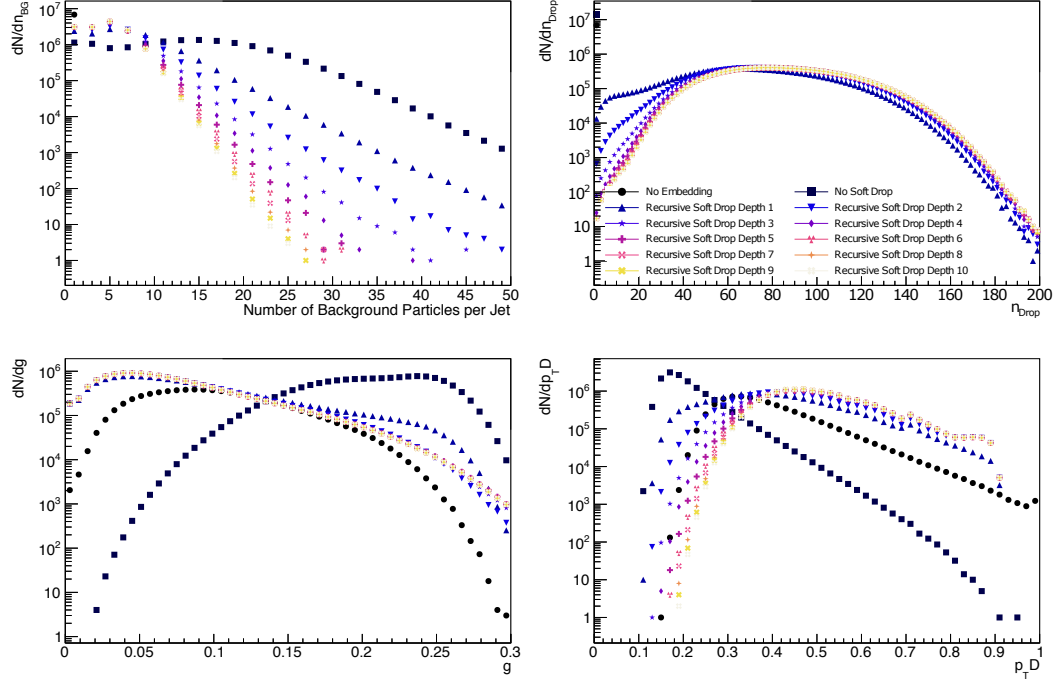


Figure 4.2: Properties of PYTHIA generated jet with  $p_T \geq 40$  GeV. In the upper panels the number of background particles per jet (left) and the number of background particles dropped from the event (right) are shown. The effect of the grooming is clearly visible. In the lower panels distributions for the jetshapes  $g$  (left) and  $p_T D$  (right) are shown. Additionally the distribution without embedding is shown. The shapes approach the non-background case with increasing number of recursions.

viation of the distribution are shown. These values grant deeper insights to the behaviour of the RSD grooming. The evolution of the distribution of  $p_{T, \text{jet}}$  is shown in the left panel of Figure 4.3. First thing to observe is the behaviour of the mean and the most probable value. Both values decrease while the most probable value decreases more strongly than the mean. This shows that the RSD first removes background particles from the jet while grooming and thus the values increase with loss of soft particles. Furthermore the standard deviation of the  $p_T$  distribution decreases with the recursive application of the Soft Drop which expresses as a narrowing of the distribution. Note that the largest share of the momentum drop appears in the first recursions. In the right panel, the moments for the momentum of the jet constituents are shown. The mean value increases with each recursion as does the standard deviation. This shows the distribution is broadening but simultaneously particles are removed so that this behaviour can be interpreted as the low momentum particle peak being successively removed. A further sign is the stability of

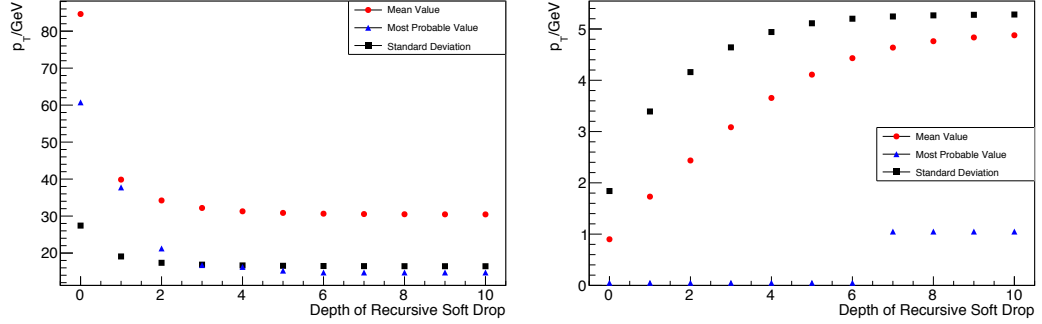


Figure 4.3:  $p_T$  of the reconstructed jets after  $n$  recursions of Soft Drop and of the according jet constituents. While the jet momentum remains mostly constant after few recursions the momentum of the constituents increases over 10 recursions.

the most probable value, which only increases slightly from a range between 0 GeV and 1 GeV to a range from 1 GeV to 2 GeV.

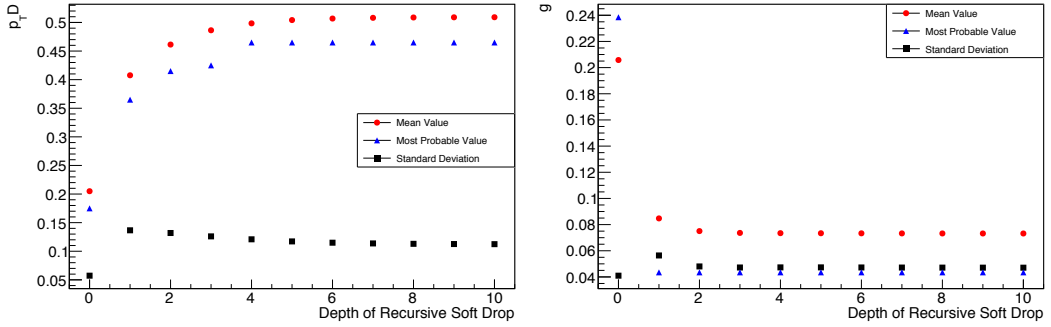


Figure 4.4: Momenta of the distributions of jetshapes  $g$  and  $p_T D$  measurements. The first recursion of grooming strongly changes the shape while the following recursions only have minor impact on the jetshapes.

As already seen in Figure 4.2 RSD has a large impact on jetshapes. Looking at the moments in Figure 4.4 gives the proof that RSD really changes the shape of the distributions. In the first step the overall distribution gets wider while the later recursions narrow them down again. Simultaneously the mean and the most probable value shift and converge to a new value with an increasing number of grooming recursions. In the left panel  $p_T D$  is shown to be shifted to larger values, while in the right panel the shift of  $g$  to lower values is shown. This is equivalent to a characteristic change of the distribution. Ungroomed distributions show a large influence of the many low  $p_T$  background particles while the groomed distributions resemble the distributions of pp collisions.

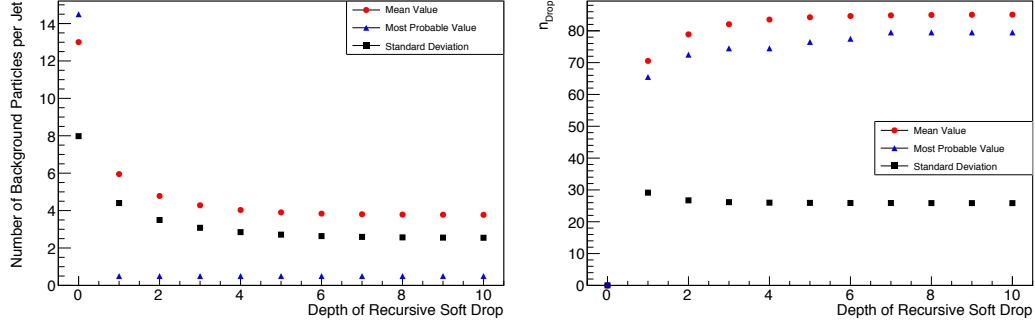


Figure 4.5: *Moments of the distributions of the number of background particles. Most jets do not contain background after one recursion while the average has an exponential reduction from 13 particles per jet to 4 particles per jet (left). The average and most probable number of particles, which got removed from the event raises up to 80 with a large standard deviation.*

For the evaluation of the grooming procedure it is interesting to have a look at the number of background particles per jet and at the number of background particles dropped from the event as shown in Figure 4.5. Starting with  $n_{BG} \approx 13$  RSD ends up with  $n_{BG} \approx 4$  thus reducing the number of background particles by a factor of three for the mean value while in the same steps the most probable value reduced from 15 to zero. Also the standard deviation of the distributions decreases, meaning that especially the number of jets with many background particles decreases strongly. The average number of particles dropped from an event increases from about 70 to more than 85 after 10 recursions. The most probable value increases from 65 to 78 with stronger increase between 4 and 7 recursions of Soft Drop. This can be interpreted as the onset on the removal of pure background jets.

Finally the distributions of the fraction of transverse momentum carried by background particles as shown in Figure 4.6 give an insight to the grooming procedure. First the amount of jets with a large fraction of background is reduced while the amount of jets with less background is enhanced. This behaviour is expected for background-reducing grooming procedures. After the fourth recursion previously unexpected behaviour sets in with jets being groomed away<sup>2</sup> which only had a small momentum fraction carried by background, while jets with large background contribution remain unchanged. To get an idea of what is happening one should remember that the Soft Drop grooming removes jets from the list if they do not fulfil the Soft Drop condition Equation 2.7 anymore. Therefore a possible explanation of this behaviour is that the jets have been groomed until only one hard parton surrounded by some background particles has remained. These jets would no longer fulfil the Soft Drop condition that requires to hard prongs in the (pseudo-)jet.

<sup>2</sup>As can be seen in the yield, these jets are completely removed from the list.

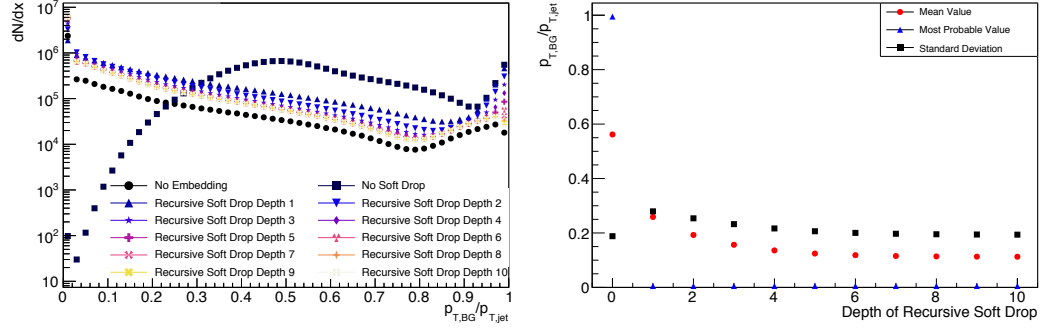


Figure 4.6: The fraction of background contributions to the reconstructed  $p_t$  of the jet reduces from 0.55 to 0.11 in an exponential decay. Most jets do not contain any background after one recursion (right). The momentum share of background reduces exponentially in a share between 0.02 and 0.8. More recursions of Soft Drop increasingly remove pure background (left).

Accordingly these jets would then be removed from the list. This assumption could be further investigated by a dedicated study, in which the constituents of the jets could be recorded at the time of removal from the list.

## 4.2 Recoil Jet Analysis with alternative FastJet Recombination Scheme

For the investigation of large angle scattering of highly energetic partons in a QGP, measurements of jets recoiling from a hard trigger hadron have been conducted. As discussed in the section on jet energy loss, partons can encounter wide angle deflection as well as large angle radiation of gluons while traversing the medium. Especially for the latter one would expect an influence of the jet recombination scheme if either the E-scheme (adding four-vectors and thus setting the jet axis in the weighted centre of all constituents) or the WTA-scheme (all momentum is added to the hardest constituent) is used. In this part of the thesis this influence will be investigated, following the analysis steps of [35]. For this analysis 2.5 million events are created as unmodified PYTHIA events as well as PYTHIA events embedded in PbPb-environment at  $\sqrt{s} = 2.76$  TeV using the `HardQCD:All` setting. For better statistics the generation is split into  $\hat{p}_T$ -bins. The embedding is implemented as described in 3.3. One further aspect of the analysis is the difference between jets originating from a quark and originating from a gluon. For this investigation two times 1.3 million events with selected processes, namely `HardQCD:all = off`, `HardQCD:gg2qqbar = on`, `HardQCD:qq2qq = on` and `HardQCD:qq2qqNew = on` for the quarks and `HardQCD:all = off`, `HardQCD:gg2gg = on` and `HardQCD:qqbar2gg = on` for the gluons accordingly, are created. The events are clustered several times with different parameters for the minimum required track transverse momentum ( $p_{t,\text{track,min}} = 0.15, 0.5, 2.0 \text{ GeV } c_0^{-1}$ ) and the jet radius parameter ( $R = 0.2, 0.4, 0.5$ ). For the different jet radii also different intervals of acceptance in  $\eta$  are required. This was also done in [35] and ensures that all possible particles inside the jet radius can be measured within the acceptance area of the a Large Heavy Ion Collider Experiment (ALICE) experiment which is  $|\eta_{\text{max}}| \leq 0.9$  [39]. The maximum values are  $|\eta_{\text{jet}}| < 0.5$  for  $R = 0.2$  and  $R = 0.4$  and  $|\eta_{\text{jet}}| < 0.4$  for  $R = 0.5$ . Furthermore a cut on the jet area is applied to suppress combinatorial jets. Jets are only accepted if their area is above a minimum value  $A_{\text{jet}} > 0.07$  if  $R = 0.2$ ,  $A_{\text{jet}} > 0.4$  if  $R = 0.4$  and  $A_{\text{jet}} > 0.6$  if  $R = 0.5$ . A comparison of the yields for these variations can give further insight to wide angle scattering and radiation as well as the influence of low energetic particles on the jet axis. For the exact comparability the same events are used for both recombination scheme analyses.

#### 4 Evaluation of Analysis Routines

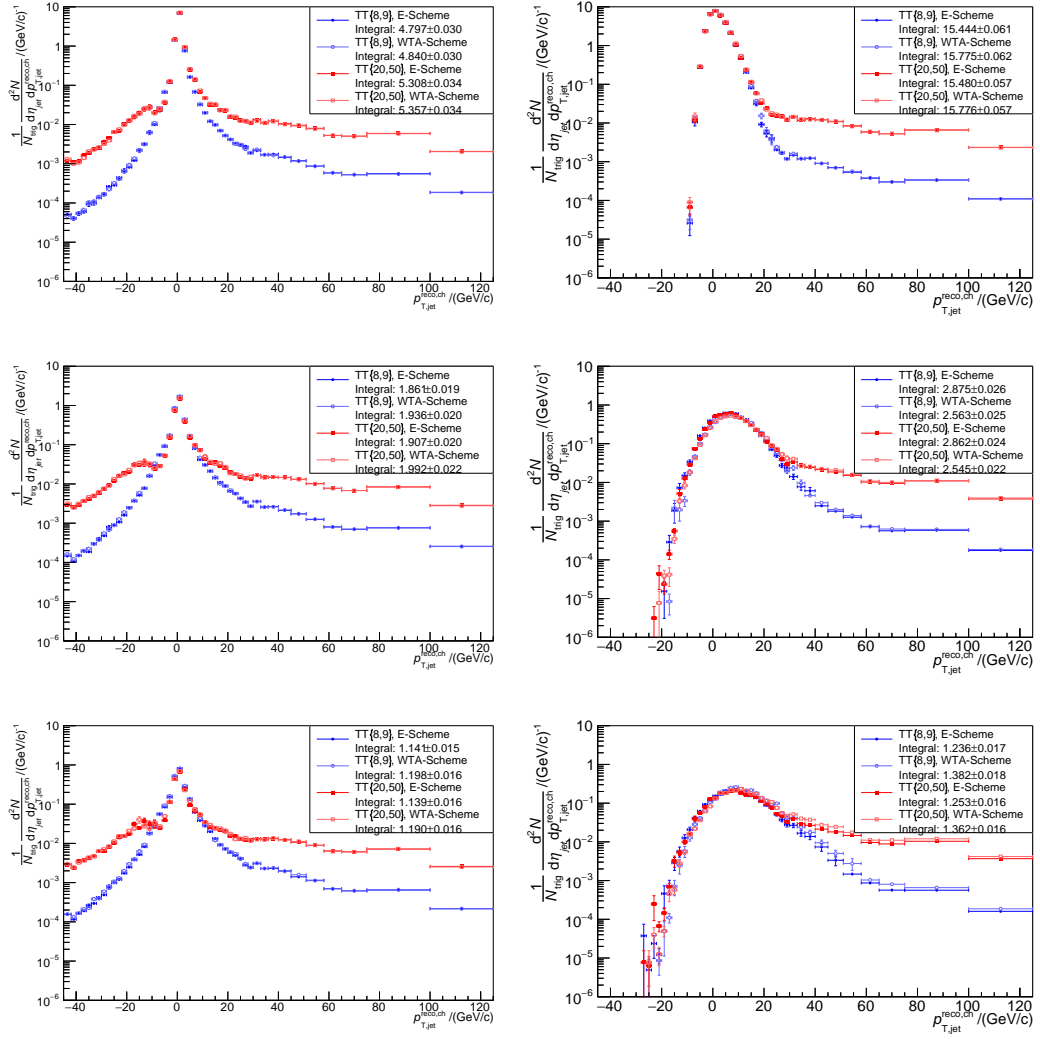


Figure 4.7: Recoil jet spectra in *PYTHIA* (left) and *PYTHIA* embedded (right) events clustered and recombined with E-scheme and WTA-scheme each. Upper panels show the yields for  $R = 0.2$ , middle panels for  $R = 0.4$  and lower panels for  $R = 0.5$ . Here  $p_{t, \text{track}, \text{min}} = 0.15 \text{ GeV } c_0^{-1}$ .

### 4.2.1 Recoil Jet Spectra and $\Delta_{recoil}$

The first step of the analysis is the comparison of the recoil jet spectra in the left panels of Figure 4.7. The signal trigger track class shows an excess in the higher  $p_T$  range in comparison with the reference trigger track class as was also observed in [35]. This is expected since the existence of a high  $p_T$  trigger hadron implies the existence of a more energetic outgoing parton in the collision. This also results in the higher yield of harder jets. There is no clear difference induced due to the choice of the recombination scheme. This can be expected, as the recombination is mainly thought to alter the angular distribution but leave the reconstructed  $p_T$  only with small changes. A similar picture is observed for PYTHIA events embedded in PbPb background as plotted in the right panels of Figure 4.7. The signal trigger class is clearly enhanced in the higher  $p_T$  region compared to the reference trigger track (TT) while there is again not much difference between the recombination schemes. It is notable though, that the yield for  $R = 0.5$  in the WTA-scheme is slightly larger than in the E-scheme. This will be further investigated in the following sections.

One aspect to note is that the position of the maximum in the spectra is slightly shifted to positive values as shown in Table 4.1. This can be interpreted as a systematic underestimation of the background density by the background subtraction methods<sup>3</sup>. This feature is also present in [35]. As listed in Table 4.1 the maximum shift is observed for large jets of  $R = 0.5$  with a small  $p_{T,track,min} = 0.15$  GeV while the shift is increasing with  $R$  and decreasing with  $p_{T,track,min}$ . The impact of background particles is expected in a similar way, since they are thought to be more abundant in larger jet areas and in general less energetic as the jet particles and thus discarded by a selection on  $p_{T,min}$ .

$p_{T,track,min} \backslash R$		0.2	0.4	0.5
0.15	GeV	1	7	9
0.5	GeV	1	5	3
2.0	GeV	1	1	3

Table 4.1: Peak positions of the recoil jet spectra recombined with E-scheme in GeV as the centre of the maximum bin. The Maximum is shifted to positive values.

---

<sup>3</sup>Remember that the two highest energetic jets are not included in the background estimation.

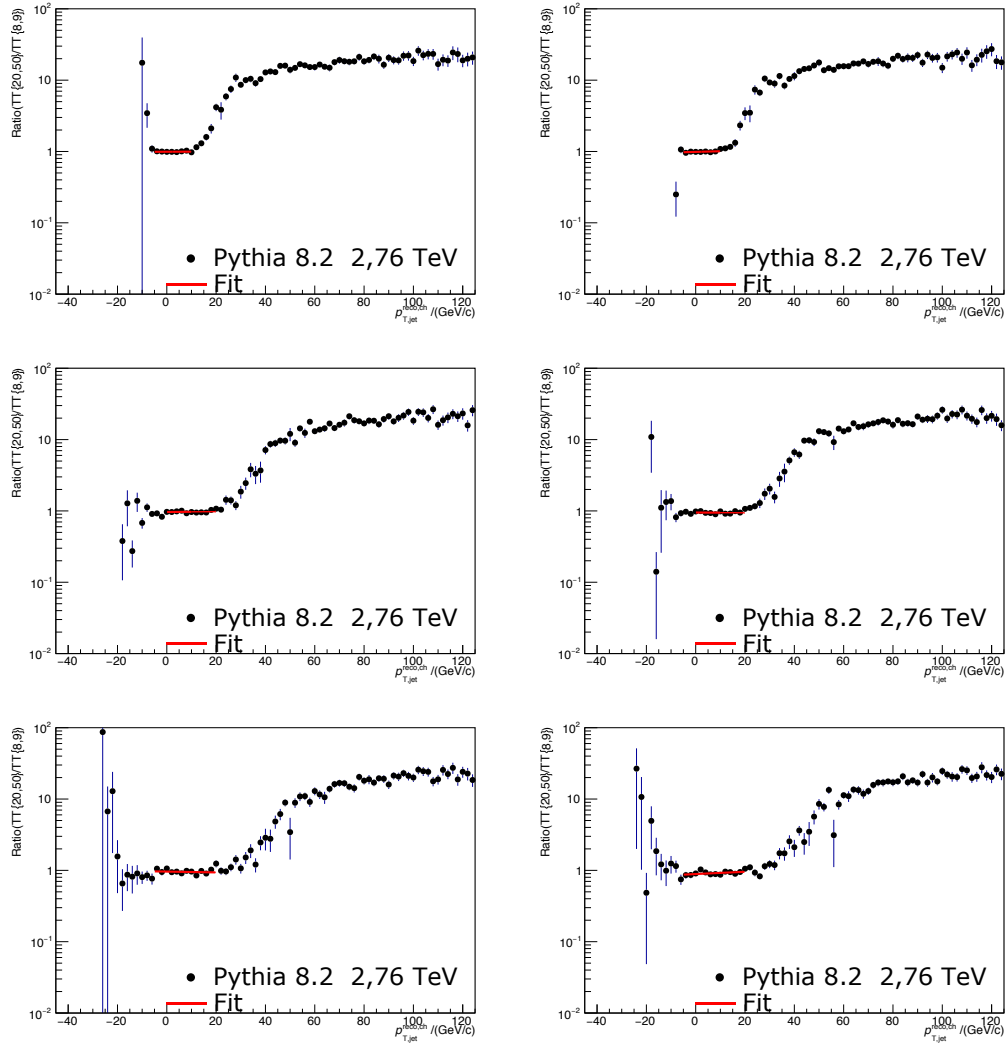


Figure 4.8: Determination of  $c_{ref}$  via the Fit (red) of the linear region of the ratio of the trigger classes for both E-Scheme (left) and WTA-Scheme (right). Upper panels show the yields for  $R = 0.2$ , middle panels for  $R = 0.4$  and lower panels for  $R = 0.5$ . Here  $p_{t,track,min} = 0.15$  GeV.



Using the ratio of the histograms Figure 4.7 as shown in Figure 4.8,  $c_{ref}$  for all combinations of jet radius parameter are calculated for both E-scheme and WTA-scheme. For this the region with the best accordance of the two trigger classes, near  $p_{T,jet} = 0$ , is fitted with a linear fit. The final values of the parameters as well as the  $\chi^2$ s are presented in Table 4.2.

$R$	$p_{T,jet}^{reco}$ fit range/GeV	Constant $c_{Ref}$ in Equation 2.10	Slope/GeV <sup>-1</sup>	$\chi^2$
0.2	[-5, 10]	$0.99 \pm 0.01$	$0.000 \pm 0.002$	4.6
		$0.99 \pm 0.01$	$0.002 \pm 0.002$	15.1
0.4	[0, 20]	$0.97 \pm 0.03$	$0.001 \pm 0.003$	6.7
		$0.95 \pm 0.03$	$0.000 \pm 0.003$	10.3
0.5	[-5, 20]	$0.96 \pm 0.04$	$-0.001 \pm 0.004$	20.0
		$0.89 \pm 0.04$	$0.003 \pm 0.003$	7.5

Table 4.2: Parameters of the linear fits to the ratio of the spectra for the two trigger classes. The upper values are for the E-scheme and the lower values for the WTA-scheme. Here  $p_{t,track,min} = 0.15$  GeV.

Note that the slope is close to zero while the constant is near unity. This again shows the good agreement of the two trigger classes below the trigger threshold where no systematic biases towards higher momenta are introduced. The fit region should be statistically identical in both trigger classes as it apparently is.

Now  $\Delta_{recoil}$  is calculated according to Equation 2.10 and plotted in Figure 4.9 with a detail plot in Figure A.2. For a better visibility the two regions are separated in two plots with suitable axis settings. In the low  $p_t$  region  $\Delta_{recoil}$  is nearly constant and in good agreement with zero, which corresponds to the already observed good agreement of the two trigger classes. Note that in the region from  $p_{T,jet}^{reco} = -10$  GeV to  $p_{T,jet}^{reco} = 10$  GeV the points for  $\Delta_{recoil}$  show a relatively large deviation from zero which is introduced due to statistical limitations. In the higher  $p_t$  range, where the distributions diverge, an exponential decay of the signal is found. Since the measurement is basically a semi-inclusive jet measurement one would expect an exponential decay towards larger momenta simply because of the exponentially decreasing cross section for the production of high  $p_t$  outgoing partons. Nonetheless this would apply to both trigger classes so that the decay seen here can be interpreted as the bias towards events with higher  $\hat{p}_t$  in the signal TT class.

For a comparison of the two recombination schemes the ratio for the three different jet radii is plotted in Figure 4.10. While the ratio for a given value of  $R$  appears to be constant an increase from  $R = 0.2$  to  $R = 0.5$  can be observed. This is again, what was already observed in Figure 4.7. This aspects need further investigation. Increased statistics as well as an analysis with more different jet radii and without a cut on the acceptance in  $\eta$  could help to a better understanding.

#### 4 Evaluation of Analysis Routines

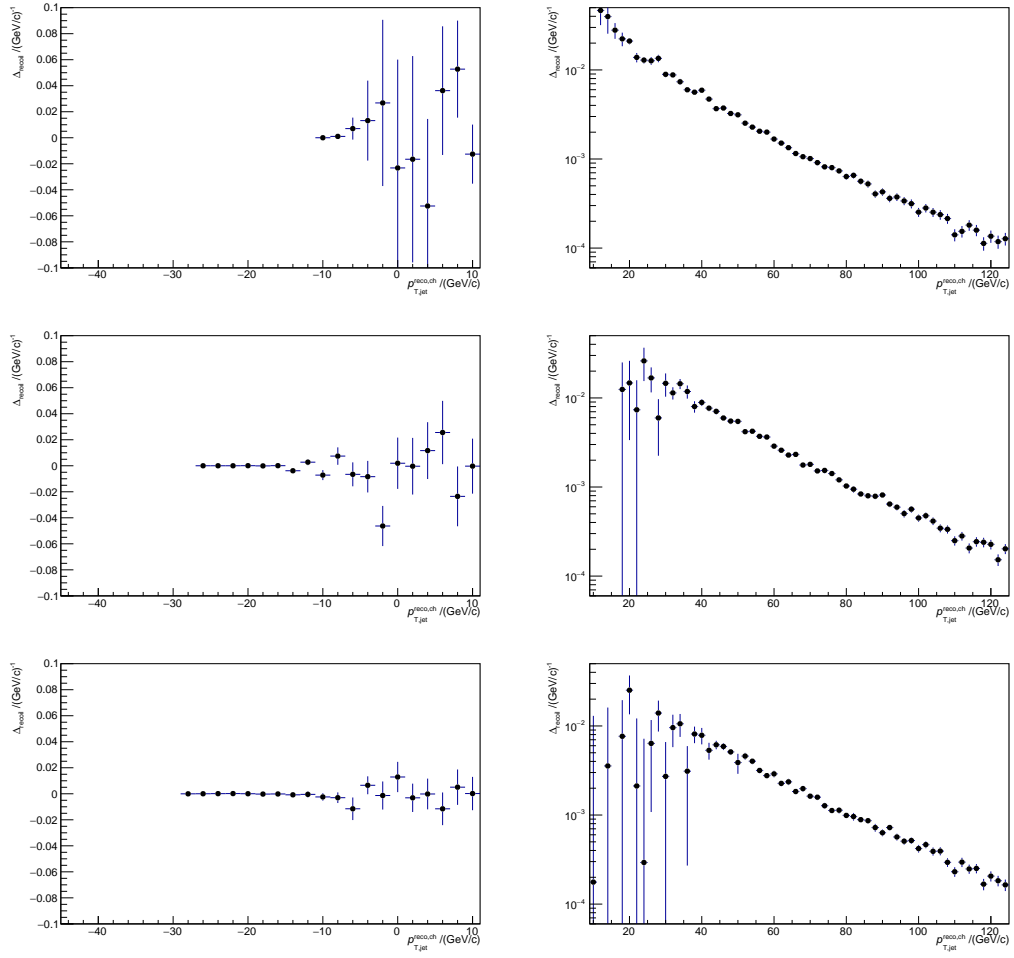


Figure 4.9:  $\Delta_{recoil}$  over the whole range of the recoil jet spectra for the spectra in E-scheme.

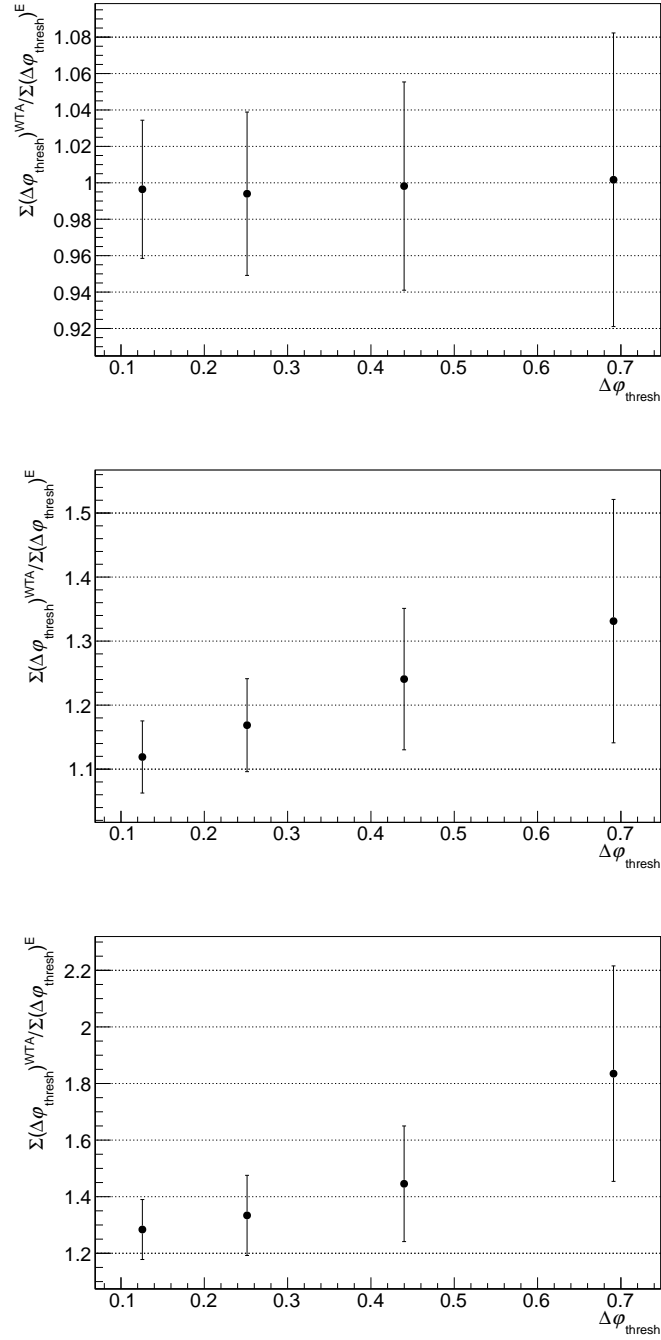


Figure 4.10: Ratio of the  $\Delta_{\text{recoil}}$  for different jet radii.

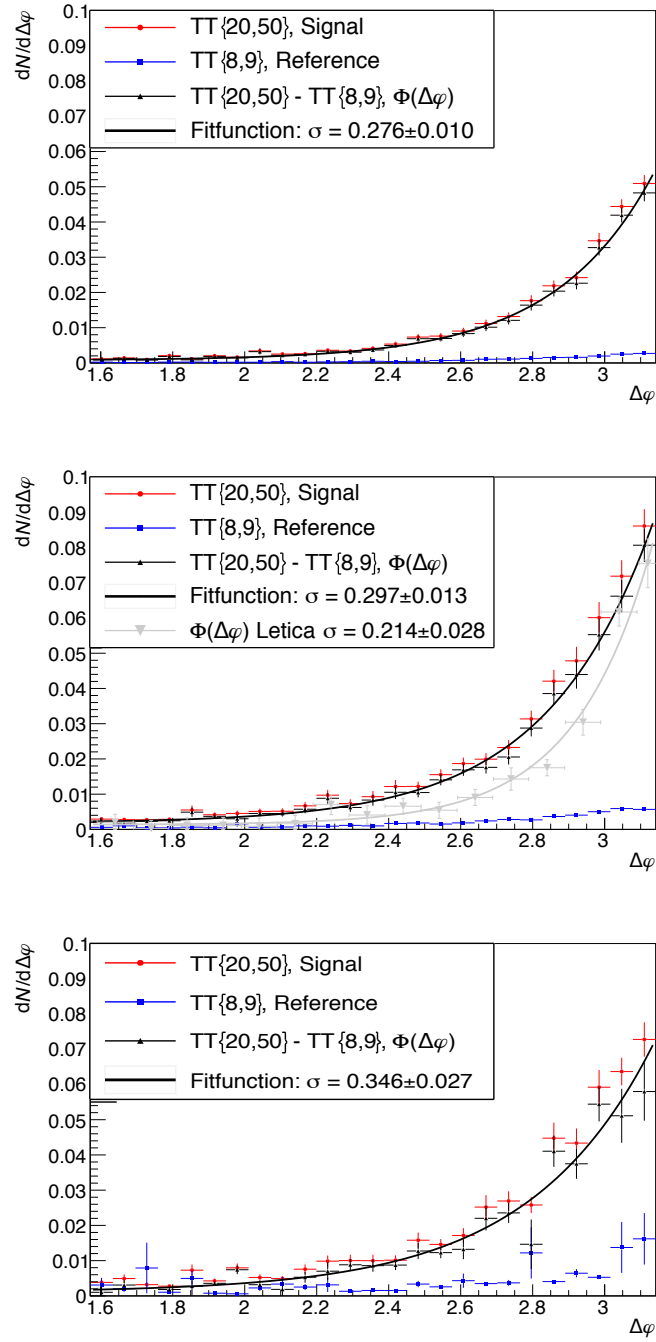


Figure 4.11: Angular distribution of the recoil jets. The distribution  $\Phi(\Delta\varphi)$  as defined in Equation 2.11 is fitted with an exponential function.

### 4.2.2 Angular Distribution and Large Angle Scattering

To further investigate large angle scattering the distribution in  $\varphi$  is examined. For this part of the analysis the same requirements for the jet as above apply but additionally, in accordance with [35], only jets with a  $40 \text{ GeV} \leq p_{\text{t reco}} \leq 60 \text{ GeV}$  are taken into account. The yield of recoil jets is plotted against the angle with respect to the trigger hadron in Figure 4.11 and using the previously determined  $c_{\text{ref}}$  the difference  $\Phi(\Delta\varphi)$  is calculated. The distributions for  $\Phi(\Delta\varphi)$  are fitted an exponential of type

$$f(\Delta\varphi) = p_0 \times e^{(\Delta\varphi - \pi)/\sigma} + p_1 \quad (4.1)$$

in a range  $2\pi/3 < \Delta\varphi < \pi$ . The fit parameters for all combinations of minimum track transverse momentum and jet radius are given in Table 4.3 and additionally in Table A.3, Table A.4 and Table A.5. Obviously there is a tendency for the distributions to broaden with increasing  $R$ , this could be a sign of transport of momentum towards larger angles. Meanwhile the widths in terms of  $\sigma$  mostly agree for both recombination schemes within the margin of error. In the mid panel additionally to the distribution created in this thesis, reference points published in [35] and the according exponential fit are shown. This distribution is „modified by the background and instrumental effects expected for central PbPb collisions“ which might be a reason why it happens to be narrower than the distribution created in this thesis. Also in [35] the distribution was fitted to  $\sigma = 0.164 \pm 0.015$  which is even narrower than the fit in this thesis.

reco.	$p_{\text{T,min}}$	$R$	$p_0$	$p_1$	$\sigma$
E	0.15	0.2	$5.42\text{e-}2 \pm 1.91\text{e-}3$	$7.32\text{e-}4 \pm 1.33\text{e-}4$	$2.76\text{e-}1 \pm 9.85\text{e-}3$
WTA	0.15	0.2	$5.38\text{e-}2 \pm 1.93\text{e-}3$	$7.90\text{e-}4 \pm 1.27\text{e-}4$	$2.73\text{e-}1 \pm 9.60\text{e-}3$
E	0.15	0.4	$8.74\text{e-}2 \pm 3.84\text{e-}3$	$1.78\text{e-}3 \pm 3.03\text{e-}4$	$2.97\text{e-}1 \pm 1.32\text{e-}2$
WTA	0.15	0.4	$8.45\text{e-}2 \pm 3.69\text{e-}3$	$1.51\text{e-}3 \pm 3.36\text{e-}4$	$3.16\text{e-}1 \pm 1.51\text{e-}2$
E	0.15	0.5	$7.18\text{e-}2 \pm 5.09\text{e-}3$	$9.65\text{e-}4 \pm 6.34\text{e-}4$	$3.46\text{e-}1 \pm 2.73\text{e-}2$
WTA	0.15	0.5	$8.14\text{e-}2 \pm 5.32\text{e-}3$	$5.13\text{e-}3 \pm 1.02\text{e-}3$	$3.02\text{e-}1 \pm 2.75\text{e-}2$

Table 4.3: Fit Values of the exponential fit to  $\Phi(\Delta\varphi)$ .

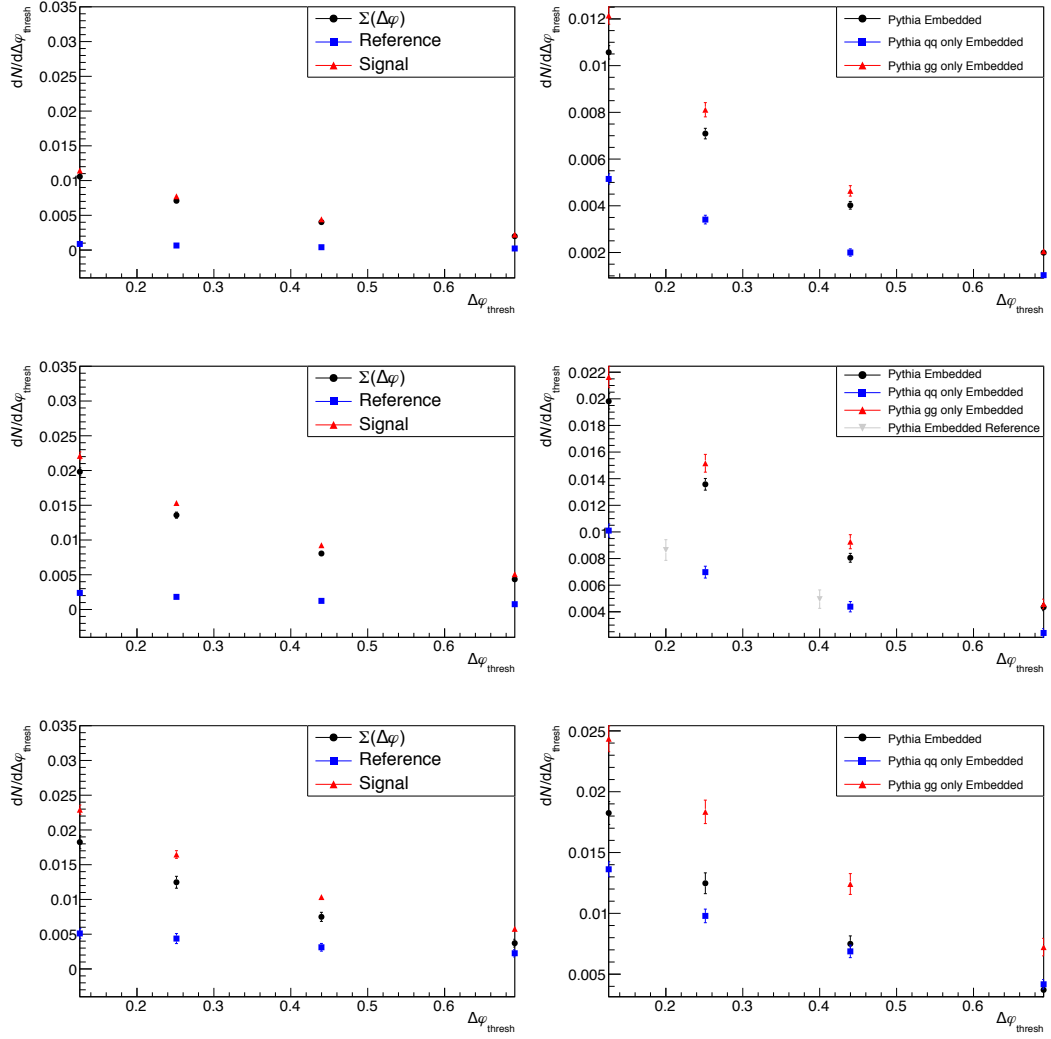


Figure 4.12:  $\Sigma(\Delta\varphi_{\text{thresh}})$  for different jet radii in the E-scheme. The left panels show the measured integrals for the reference and signal TT class as well as the resulting values for  $\Sigma(\Delta\varphi_{\text{thresh}})$ . The right panels show the results for  $\Sigma(\Delta\varphi_{\text{thresh}})$  for different event generation routines using `HardQCD:all` and `gg` as well as `qq` events only. One can see that the distributions for quark and gluon jets differ strongly. The upper panels are for  $R = 0.2$ , the mid panels for  $R = 0.4$  and the lower panels for  $R = 0.5$ . Additionally in the right mid panel the reference points from [35] are shown.

The tail of the distribution on  $\varphi$ , i.e. the yield of wide angle scattering, can be measured by integration up to a certain threshold value  $\Sigma(\Delta\varphi_{\text{thresh}})$ . This is also evaluated for a wide range of parameters, examples for the construction of  $\Sigma(\Delta\varphi_{\text{thresh}})$  are shown in the left panels of Figure 4.12. The right panels show examples for the comparison of the three different event generation settings in this analysis. One can see that the graphs strongly deviate for the different settings. The yield per trigger hadron for jets originating from a gluon is in general larger than the yield for jets originating from a quark even though the overall yield for recoil jets per trigger hadron is similar within the margin of error. This aspect could not be understood in this thesis and needs further investigation. Also the yield generated in this thesis is larger than the one in [35]. This can be again due to instrumentation effects regarded in [35] and not in this thesis as well as different intervals for the integration. In general the shape of the graph is comparable to the published reference.

Finally the  $\Sigma$  as defined in Equation 2.12 of the two different jet recombination schemes can be compared. An enhancement of jets towards larger  $\Delta\varphi_{\text{thresh}}$  is observed for the WTA recombination scheme relative to the E-scheme for jets with radius parameter  $R = 0.4$  and  $R = 0.5$ . Obviously when combined with the WTA-scheme jets have a tendency to be localised further away from a back-to-back recoil. This can be interpreted as increased sensitivity of analyses utilising the WTA-scheme for large angle scattering and is (within the understanding of the author) in agreement with the results for recoil jet spectra where an excess of jets for larger  $R$  was observed.

This effect can also be resolved for quarks and gluons as outgoing partons as shown in Figure 4.13. In this analysis only quark jets are clearly enhanced at large  $\Delta\varphi_{\text{thresh}}$  in the WTA-scheme, while for gluon jets the situation is unclear. For  $R = 0.4$  the yield is increased for all  $\Delta\varphi_{\text{thresh}}$  with no clear distinction between quark and gluon jets. For  $R = 0.5$  it is clear, that only quark jets contribute to the increase of the WTA-scheme while the yield for gluon jets does not favour any recombination scheme. This is in compatible to the earlier finds of gluon jets fragmenting broader and more evenly than quark jets. If the momentum of the jet is more evenly distributed in the jet cone one would expect the WTA-scheme as well as the E-scheme to recombine a well centred jet. In the case of more unevenly fragmenting quark jets the WTA-scheme should reconstruct jets biased strongly to the heavier fragment, resulting in generally broader angular distribution.

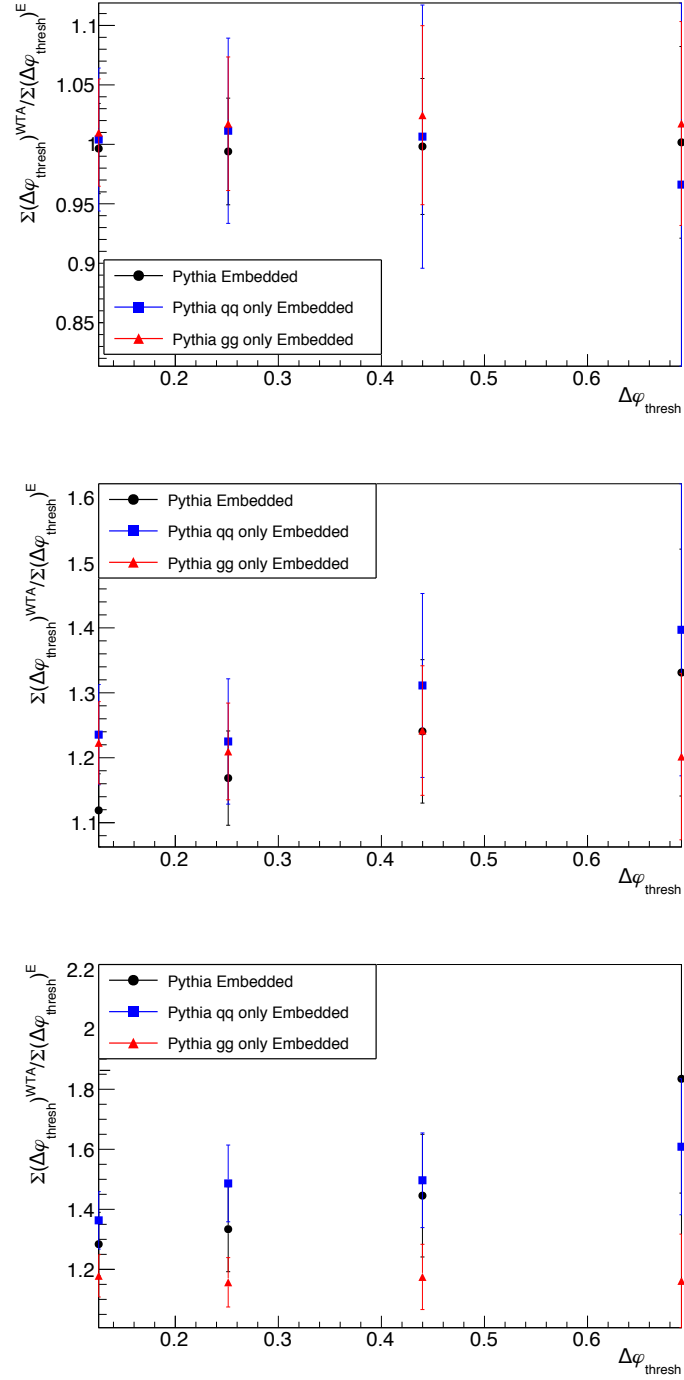


Figure 4.13: Ratio of the  $\Sigma(\Delta\varphi_{\text{thresh}})$  of the different recombination schemes.



### 4.3 Lund Plane Analysis with Background Toy Model

The third analysis method examined in this thesis is the influence of combinatorial background on the *Lund plane* representation of jets. For this analysis 1.5 million events in 15  $\hat{p}_t$ -bins are created using the JETSCAPE framework using the default settings of version 3.1. This means the events are set up by TRENTO, the nucleon collisions are handled by the PYTHIA collision kernel and the medium modifications as well as the hadronisation are calculated by MATTER. For PYTHIA the setting is the basic `HardQCD:all = on` processes, with the according range in  $\hat{p}_t$ . MATTER is set up with a transport parameter  $\hat{q} = 2.0$ , and  $\alpha_s = 0.2$ . The brick length is set to 5.0

In the analysis three different stages of background are implemented.

- No background at all, only the medium modifications from MATTER. This can be understood as a reference to the background influence.
- *Global* background to the whole event. Jet finding is executed after the background is added, so that additionally to the jet modifications by background also combinatorial background jets are possible.
- *Local* background, which is only added to already clustered jets. This can be regarded as an intermediate background contribution to investigate the influence of background to the jet clustering history in a very clean environment which is not contaminated with combinatorial jets.

Furthermore the possibility to extract certain regions of the *lund plane* via jet grooming with Soft Drop ( $\beta = 0.0$ ,  $z_{\text{cut}} = 0.25$ ) and geometrical cuts are regarded. Figure 4.14 shows the *Lund planes* for the three different background creation routines without modifications and with Soft Drop applied. The histograms are scaled to a relative density for a better comparison of the different settings.

Embedding the event in additional background as expected from PbPb collisions clearly changes the relative abundance of splittings in the jets. The splittings are spread out further in the phase space. On the right panels the *Lund planes* are shown after application of Soft Drop are shown. As discussed in section 2.3 Soft Drop removes splittings in the low  $\ln(k_t)$  and low  $\ln(1/\Delta)$  region. Nonetheless some splittings in this region are not groomed, in contrast to a geometric cut, which removes all the splittings. The red lines represent cuts of this kind, where only splittings are kept, which fulfill  $\ln(k_t) > c_{\text{textcut}} - \ln(1/\Delta)$ . For the analysis  $c_{\text{cut}} = [-1.5, 0.5]$  are used. As shown in Figure 4.14 the geometric cuts discussed in this thesis remove at least parts of the region of the largest density. This region contains mostly soft-collinear and initial state radiation. For the investigation of hard jet fragmentation the remaining area contains the important information.

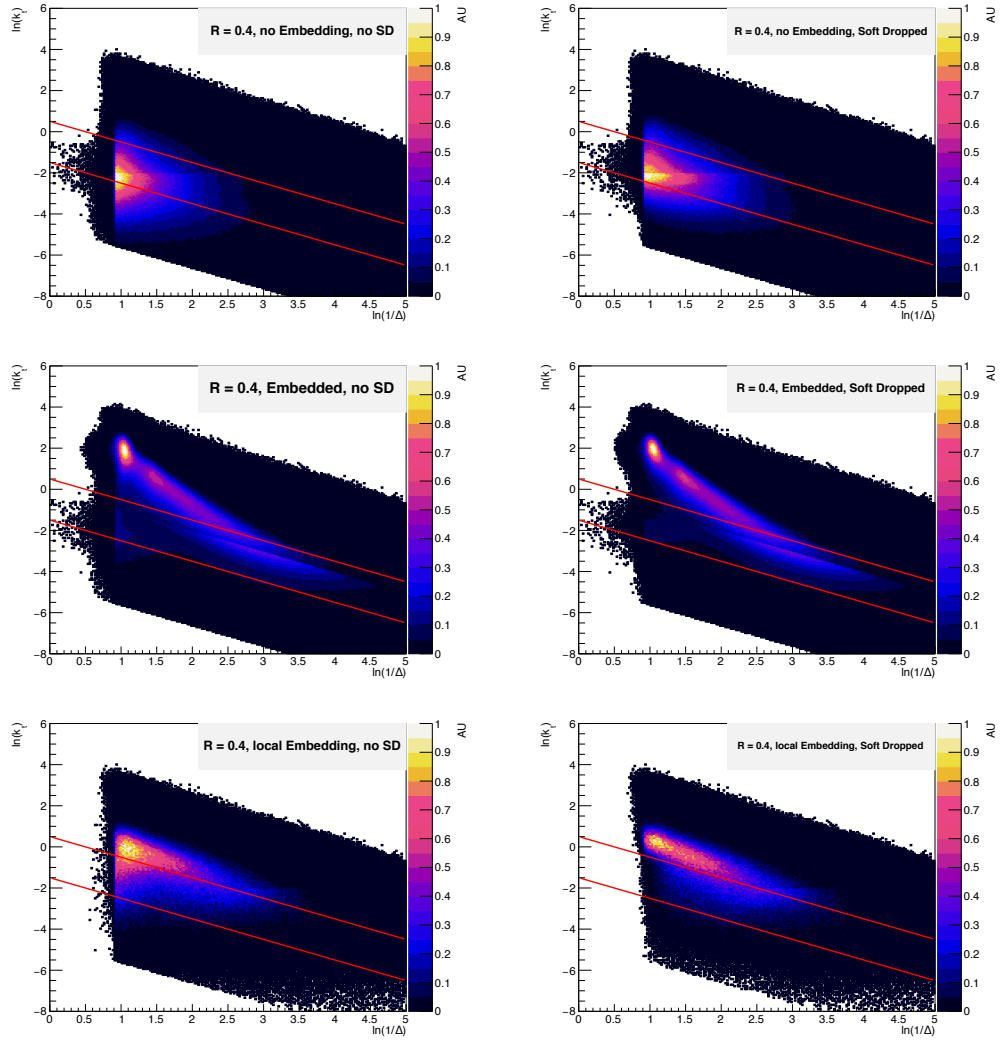


Figure 4.14: Lund plane diagrams for the different settings of background and Soft Drop. The diagonal lines represent manually chosen cuts, which are applied for further analysis.

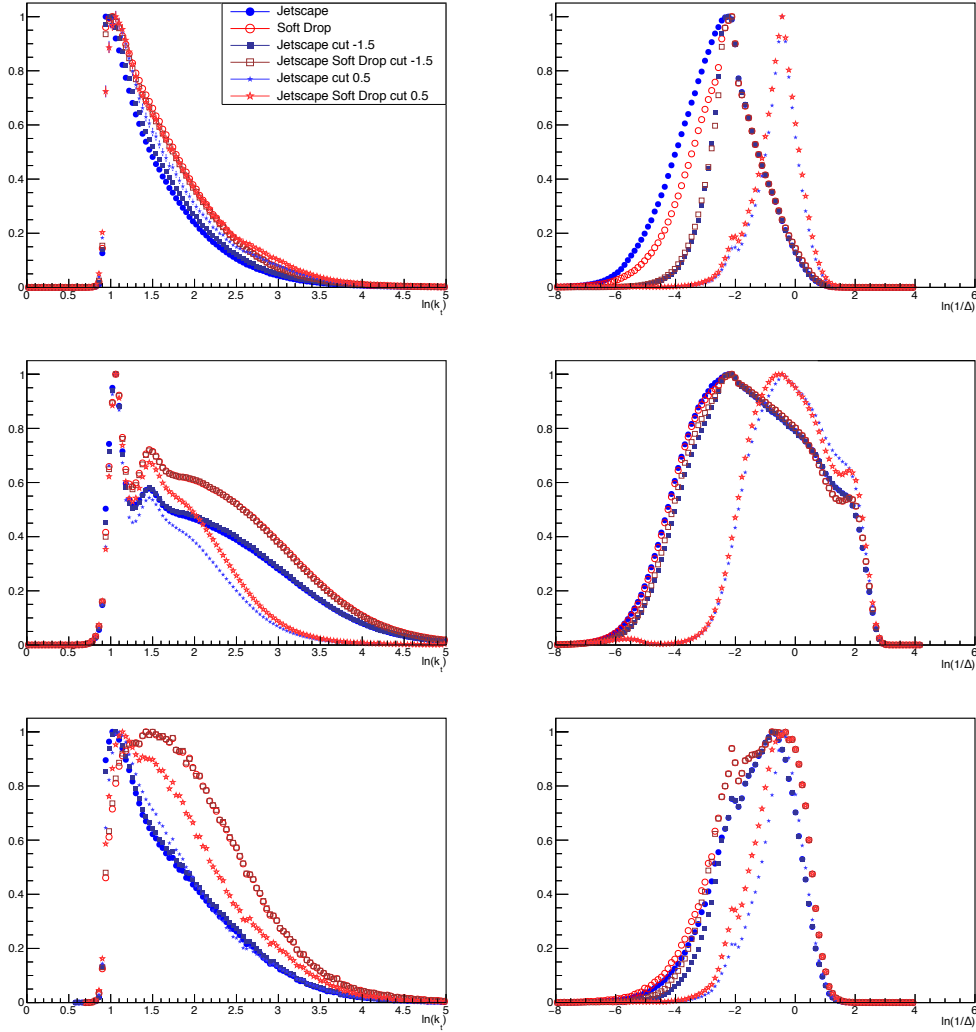


Figure 4.15: Projections of the Lund plane density to the x-axis (left panels) and the y-axis (right panels). The influence of the background is clearly visible. Soft Drop and wide cuts have comparable effects on the distributions, and if applied simultaneously show effects similar to a tighter cut. The legend from the top left panel applies to all panels as well.

For a more detailed analysis the projections on both axes are regarded. All distributions are scaled to the same height for easier comparability. As already seen in the 2D representation the shapes differ for the different background creation routines. Compared to no embedding the *Lund diagrams* for the local embedding show a similar distribution in both axes. The strong deviation observed for the global embedding can thus be interpreted as

the influence of combinatorial background jets. Note that the distributions in  $\ln(k_t)$  become broader after the application of Soft Drop, while the influence of background jets is only partially removed. Only a tight cut on the upper section of the *Lund plane* leads toward the shape of the projection without background. The shapes of the projection on  $\ln(1/\Delta)$  are mostly left unchanged by the application of Soft Drop, which was expected by the definition. Here it can be seen, that cuts shift the distribution towards larger values as progressively more entries get removed. The shapes of the projection on  $\ln(k_t)$  are strongly modified by the application of Soft Drop. Compared to no application of Soft Drop and to no embedding the distributions are shifted to larger values (only jets embedded) and show enhanced background contribution (event embedded). The cut on  $z_g = 0.25$  does not seem to remove background particles in the first place but also cuts on original jet splittings. Geometrical cuts seem to have a larger potential to remove background contributions from the *Lund plane* for both types of embedding. The performance of geometrical cuts on background removal surprises on the first impression since it also partially removes the regions of the largest densities in the diagrams with no embedding. On the second impression this can be solved, remembering that in this region soft splittings are represented. It would be promising though to further investigate and optimise the capabilities of Soft Drop and its recursive offsprings <sup>4</sup> for grooming the *Lund plane*.

---

<sup>4</sup>Recursive Soft Drop and Iterative Soft Drop

---

## 5 Summary and Outlook

After the three quite different analyses this chapter will provide a short summary and will frame the results in a larger picture. It will also provide a short outlook on the impact of the results and potential upcoming analyses. The evaluation of the RSD has shown that grooming can be a strategy for background reduction in high multiplicity environments in a way that leaves a lot of the kinematics of the jet unchanged but solely removes uncorrelated background particles. An optimum for the recursion depth can be deducted at around five recursions, as the background removal saturates and more recursions start to alter other kinematic observables. In the second part, the influence of the recombination scheme on angular analyses was evaluated. The differences only show up in direct comparison of the two recombination schemes used. Yet it is important to note, that for the research on large angle scattering, WTA-recombination might yield an enhanced sensitivity. Since the study was only done with PYTHIA embedded events further investigations with event generators, which emphasise further aspects of heavy ion collisions could help to complete the view. One possible event generator could be the JETSCAPE framework, which was tested in the third study. In version 3 the handling of JETSCAPE improved a lot compared to earlier versions, which still needed considerable manual work to get started. The recent versions feature clear workflows for the generation and analysis of events in a clean docker environment for quick installation. In this study the representation of jet splittings in the *Lund plane* was examined. The influence of background on the relative density was presented. It could be shown that purely combinatorial jets can significantly change the distribution of splittings in the *Lund* representation. Additionally it could be shown that grooming with the Soft Drop procedure can have effects similar to geometrical cuts. This is an important finding since Soft Drop is mathematically well defined while geometrical cuts are harder to propagate in theoretical calculations for jet observables.

This thesis has ruled out several options for optimising existing analyses and additionally has shown possibilities for future research. It also provides first insights and information for such. Starting from the findings in this thesis, further studies on the angular distribution of recoil jets seem a promising field of research. These investigations could be backed up with a JETSCAPE reference to improve the differentiation of different medium effects.



# A Additional plots and tables

## A.1 Background Reduction for Jetshape Observables

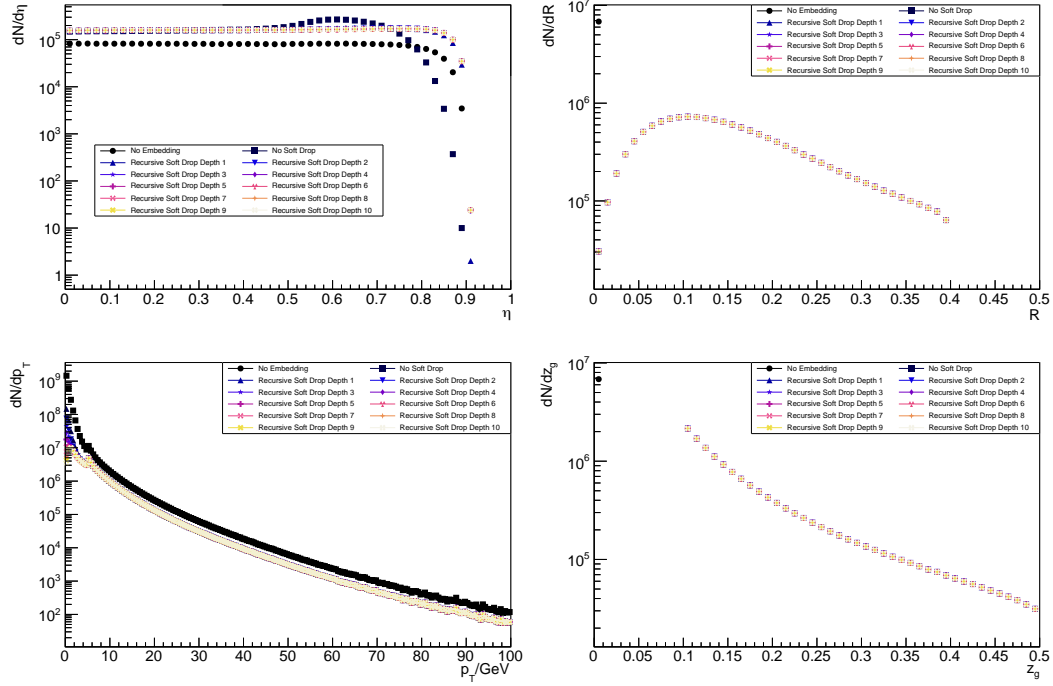


Figure A.1: Properties of PYTHIA generated jet with  $p_T \geq 40$  GeV. In the upper panels the pseudorapidity of the jets (left) and the radial distance of the analysed splittings (right) are shown. In the lower panels distributions for the transverse momentum of the single particles (left) and the momentum fraction  $z_g$  (right) are shown. Additionally the distribution without embedding is shown.

## A.2 Recoil Jet Analysis with alternative FastJet Recombination Scheme

$R$	$p_{T,\text{jet}}^{\text{reco}}$ fit range in GeV	Constant $c_{\text{Ref}}$ in Equation 2.10	Slope in $\text{GeV}^{-1}$	$\chi^2$
0.2	[-5, 10]	$0.98 \pm 0.01$	$0.003 \pm 0.002$	8.7
		$0.98 \pm 0.01$	$0.004 \pm 0.002$	22.9
0.4	[0, 20]	$0.91 \pm 0.03$	$0.006 \pm 0.003$	19.6
		$0.93 \pm 0.03$	$0.002 \pm 0.003$	25.4
0.5	[-5, 20]	$0.93 \pm 0.03$	$0.003 \pm 0.004$	14.6
		$0.91 \pm 0.03$	$0.002 \pm 0.003$	5.4

Table A.1: Parameters of the linear fits to the ratio of the spectra for the two trigger classes. The upper values are for the E-scheme and the lower values for the WTA-scheme. Here  $p_{t,\text{track,min}} = 0.5 \text{ GeV}$ .

$R$	$p_{T,\text{jet}}^{\text{reco}}$ fit range in GeV	Constant $c_{\text{Ref}}$ in Equation 2.10	Slope in $\text{GeV}^{-1}$	$\chi^2$
0.2	[-5, 10]	$0.97 \pm 0.01$	$0.010 \pm 0.004$	35.6
		$0.97 \pm 0.02$	$0.010 \pm 0.004$	68.6
0.4	[0, 20]	$0.87 \pm 0.03$	$0.020 \pm 0.004$	172
		$0.91 \pm 0.03$	$0.012 \pm 0.005$	241
0.5	[-5, 20]	$0.88 \pm 0.03$	$0.012 \pm 0.004$	72.9
		$0.89 \pm 0.03$	$0.010 \pm 0.004$	64.9

Table A.2: Parameters of the linear fits to the ratio of the spectra for the two trigger classes. The upper values are for the E-scheme and the lower values for the WTA-scheme. Here  $p_{t,\text{track,min}} = 2.0 \text{ GeV}$ .



## A.2 Recoil Jet Analysis with alternative FastJet Recombination Scheme

recomb.	$p_{T,\min}$	$R$	$p_0$	$p_1$	$\sigma$
E	0.50	0.2	$5.35\text{e-}2 \pm 1.95\text{e-}3$	$8.40\text{e-}4 \pm 1.19\text{e-}4$	$2.63\text{e-}1 \pm 9.02\text{e-}3$
WTA	0.50	0.2	$5.41\text{e-}2 \pm 2.01\text{e-}3$	$8.37\text{e-}4 \pm 1.17\text{e-}4$	$2.60\text{e-}1 \pm 8.85\text{e-}3$
E	0.50	0.4	$8.23\text{e-}2 \pm 3.70\text{e-}3$	$1.66\text{e-}3 \pm 2.78\text{e-}4$	$2.89\text{e-}1 \pm 1.34\text{e-}2$
WTA	0.50	0.4	$8.69\text{e-}2 \pm 3.41\text{e-}3$	$1.67\text{e-}3 \pm 2.98\text{e-}4$	$3.14\text{e-}1 \pm 1.29\text{e-}2$
E	0.50	0.5	$6.78\text{e-}2 \pm 2.76\text{e-}3$	$1.39\text{e-}3 \pm 3.54\text{e-}4$	$3.49\text{e-}1 \pm 1.78\text{e-}2$
WTA	0.50	0.5	$6.64\text{e-}2 \pm 5.60\text{e-}3$	$1.36\text{e-}3 \pm 7.29\text{e-}4$	$3.61\text{e-}1 \pm 3.39\text{e-}2$
E	2.00	0.2	$4.87\text{e-}2 \pm 1.72\text{e-}3$	$8.28\text{e-}4 \pm 1.13\text{e-}4$	$2.68\text{e-}1 \pm 9.25\text{e-}3$
WTA	2.00	0.2	$4.61\text{e-}2 \pm 1.71\text{e-}3$	$5.96\text{e-}4 \pm 1.06\text{e-}4$	$2.70\text{e-}1 \pm 9.75\text{e-}3$
E	2.00	0.4	$6.17\text{e-}2 \pm 2.05\text{e-}3$	$9.71\text{e-}4 \pm 1.59\text{e-}4$	$2.78\text{e-}1 \pm 9.70\text{e-}3$
WTA	2.00	0.4	$5.82\text{e-}2 \pm 2.02\text{e-}3$	$8.49\text{e-}4 \pm 1.56\text{e-}4$	$2.79\text{e-}1 \pm 1.04\text{e-}2$
E	2.00	0.5	$5.37\text{e-}2 \pm 2.12\text{e-}3$	$8.58\text{e-}4 \pm 1.46\text{e-}4$	$2.76\text{e-}1 \pm 1.09\text{e-}2$
WTA	2.00	0.5	$5.10\text{e-}2 \pm 2.16\text{e-}3$	$7.70\text{e-}4 \pm 1.57\text{e-}4$	$2.83\text{e-}1 \pm 1.24\text{e-}2$

Table A.3: Fit Values of the exponential fit to  $\Phi(\Delta\varphi)$ , for the events generated with *HardQCD : a11*

recomb.	$p_{T,\min}$	$R$	$p_0$	$p_1$	$\sigma$
E	0.15	0.2	$2.75\text{e-}2 \pm 1.41\text{e-}3$	$2.88\text{e-}4 \pm 7.30\text{e-}5$	$2.63\text{e-}1 \pm 1.37\text{e-}2$
WTA	0.15	0.2	$2.96\text{e-}2 \pm 1.50\text{e-}3$	$3.65\text{e-}4 \pm 6.85\text{e-}5$	$2.47\text{e-}1 \pm 1.21\text{e-}2$
E	0.15	0.4	$4.29\text{e-}2 \pm 2.49\text{e-}3$	$6.51\text{e-}4 \pm 2.05\text{e-}4$	$2.94\text{e-}1 \pm 1.96\text{e-}2$
WTA	0.15	0.4	$5.56\text{e-}2 \pm 2.90\text{e-}3$	$1.57\text{e-}3 \pm 2.12\text{e-}4$	$2.66\text{e-}1 \pm 1.52\text{e-}2$
E	0.15	0.5	$4.30\text{e-}2 \pm 2.97\text{e-}3$	$1.68\text{e-}3 \pm 3.83\text{e-}4$	$3.31\text{e-}1 \pm 3.14\text{e-}2$
WTA	0.15	0.5	$5.09\text{e-}2 \pm 3.32\text{e-}3$	$2.94\text{e-}3 \pm 5.96\text{e-}4$	$3.35\text{e-}1 \pm 3.09\text{e-}2$

Table A.4: Fit Values of the exponential fit to  $\Phi(\Delta\varphi)$ , for only quark jets.

recomb.	$p_{T,\min}$	$R$	$p_0$	$p_1$	$\sigma$
E	0.15	0.2	$5.42\text{e-}2 \pm 2.30\text{e-}3$	$6.51\text{e-}4 \pm 1.90\text{e-}4$	$2.97\text{e-}1 \pm 1.27\text{e-}2$
WTA	0.15	0.2	$5.42\text{e-}2 \pm 2.25\text{e-}3$	$7.12\text{e-}4 \pm 2.10\text{e-}4$	$2.94\text{e-}1 \pm 1.29\text{e-}2$
E	0.15	0.4	$8.15\text{e-}2 \pm 4.26\text{e-}3$	$1.70\text{e-}3 \pm 4.67\text{e-}4$	$3.22\text{e-}1 \pm 1.85\text{e-}2$
WTA	0.15	0.4	$9.06\text{e-}2 \pm 4.00\text{e-}3$	$1.61\text{e-}3 \pm 4.62\text{e-}4$	$3.33\text{e-}1 \pm 1.62\text{e-}2$
E	0.15	0.5	$7.31\text{e-}2 \pm 5.27\text{e-}3$	$2.43\text{e-}3 \pm 9.61\text{e-}4$	$3.63\text{e-}1 \pm 3.71\text{e-}2$
WTA	0.15	0.5	$7.78\text{e-}2 \pm 4.05\text{e-}3$	$2.18\text{e-}3 \pm 9.06\text{e-}4$	$3.93\text{e-}1 \pm 3.05\text{e-}2$

Table A.5: Fit Values of the exponential fit to  $\Phi(\Delta\varphi)$ , for only gluon jets.

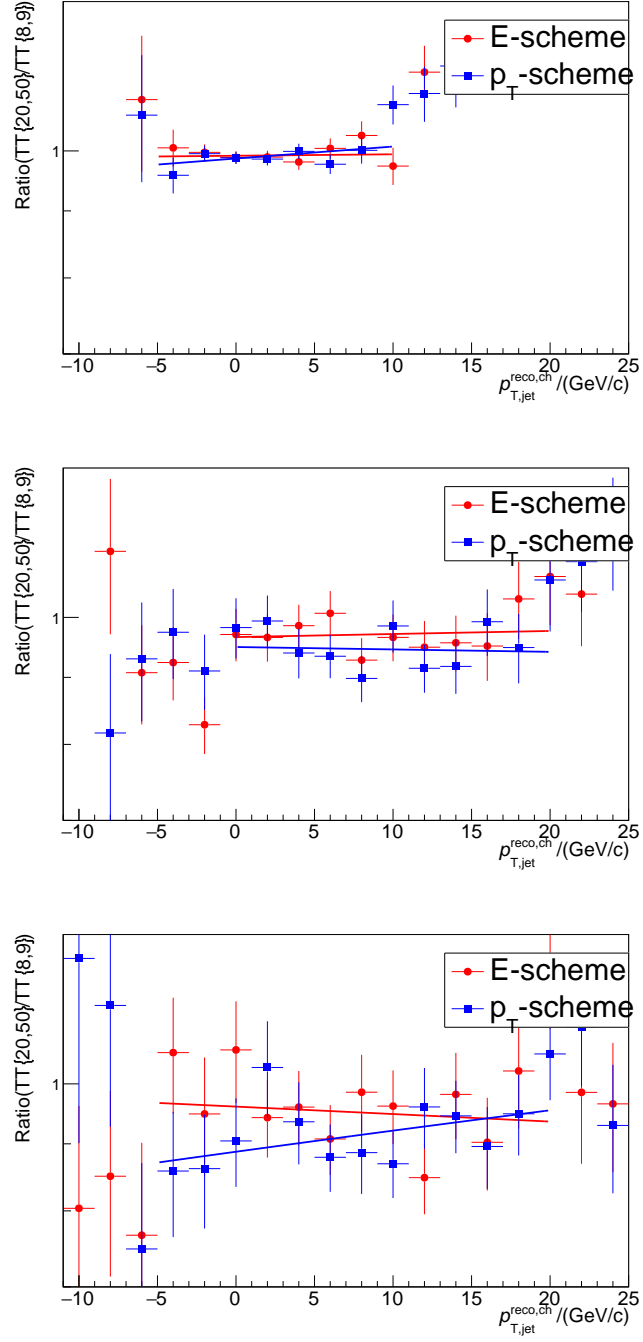


Figure A.2: Ratio of the recoil jet spectra for different jet radii, zoomed to the fitted area and on linear axis setting. The top panel shows  $R = 0.2$ , the mid panel shows  $R = 0.4$  and the bottom panel shows  $R = 0.5$ . Here  $p_{t,track,min} = 0.15$  GeV

---

## B How to JETSCAPE

This appendix gives a short guide how to install and use JETSCAPE to generate and analyse events. A full description of the JETSCAPE modules is given in [] so here the focus is laid on the practical aspects. This short manual focuses on Unix like systems, so if you try to set up JETSCAPE on a Windows machine you will likely have to adapt to your system.

### B.1 Installing JETSCAPE

For getting started with JETSCAPE the easiest way of installation is to install the JETSCAPE DOCKER container that is supplied by the collaboration <https://github.com/JETSCAPE/JETSCAPE/tree/master/docker>. The steps are as follows:

1. Download and install docker for your operating system from:

<https://docs.docker.com/get-docker/>

2. Get JETSCAPE working:

- a) Make a directory on your computer for JETSCAPE and move into it:

```
$ mkdir ~/jetscape-docker
$ cd ~/jetscape-docker
```

- b) Download JETSCAPE from Git into the directory:

```
$ git clone https://github.com/JETSCAPE/JETSCAPE.git
```

- c) Create and start the docker container for your JETSCAPE installation.

Mac:

```
$ docker run -it
-v ~/jetscape-docker:/home/jetscape-user
--name myJetscape jetscape/base:v1.4
```

Linux:

```
$ docker run -it
-v ~/jetscape-docker:/home/jetscape-user
--name myJetscape
--user $(id -u):$(id -g) jetscape/base:v1.4
```

Familiarise yourself with the basics of Docker. This can come in handy while the usage of JETSCAPE. Also note, that the version numbers might change.

- d) Build JETSCAPE inside the Docker container.

```
$ cd JETSCAPE
$ mkdir build
$ cd build
$ cmake ..
$ make -jn
```

with *n* being the number of cores that you want to use for the compilation. This can take some while.

After this is done JETSCAPE is built and can be used. For example the JETSCAPE example programs should be able to run now. Try:

```
$ cd JETSCAPE/build
$ ./runJetscape ../config/jetscape_user_PP19.xml
```

This programme will run for some time now and create a `.hepmc` file. From here you can start using JETSCAPE.

3. An easier way to use JETSCAPE is via the python interface  
<https://github.com/jdmulligan/JETSCAPE-analysis>.  
Go outside Docker and download the JETSCAPE-analysis folder from git:

```
$ cd ~/jetscape-docker/
$ git clone git@github.com:
    jdmulligan/JETSCAPE-analysis.git
```

## B.2 Running JETSCAPE

From inside docker you can now go to the folder

```
$ cd jetscape_analysis/generate
```

and execute the python script

```
$ python jetscape_events.py  
-c /home/jetscape-user/JETSCAPE-analysis/config/example.yaml  
-o /home/jetscape-user/JETSCAPE-analysis-output
```

where `-c` specifies a config file and `-o` specifies the output location.

This is a basic test script for the creation of JETSCAPE events. In general simulations using JETSCAPE are analysed in a two stage process where events are created according to the users settings and analysed in a second step. This is a useful routine since the creation of events with JETSCAPE takes some while.

To adapt and customise the event creation there are several places to do so.

1. .yaml files
2. .xml files
3. .py generation script

The JETSCAPE collaboration provides tunes for  $pp$  collisions and is currently working on tunes for  $PbPb$  collisions. Some default settings are given in a master file in JETSCAPE/config/jetscape\_master.xml Here you can also create a user config file to create events according to your settings. Just copy the example user file and edit it to your needs. More information is given in the talks for the JETSCAPE Summer School 2020.<sup>1</sup>

In any case you can always use the python script for launching the event generation.

---

<sup>1</sup><https://indico.bnl.gov/event/8660/timetable/>

### B.3 Analysing JETSCAPE events

To analyse the events which are now created another python script can be used. For a basic analysis an example script is provided which can be executed with:

```
$ cd /home/jetscape-user/JETSCAPE-analysis /
    jetscape_analysis/analysis
$ python analyze_events_example.py
  -c ../../config/example.yaml
  -i /home/jetscape-user/JETSCAPE-analysis-output
  -o /my/outputdir
```

where again `-c` specifies a config file, `-i` the input location where the events are stored and `-o` specifies the output location.

To create analysis routines you should write your personal analysis class which inherits from the base class

`jetscape_analysis/analysis/analyze_events_base.py`.

You need to implement a function called `initialize_user_output_objects()` and a function called `analyze_events(event)`. An example is also given in the folder.

---

# Bibliography

- [1] K. Adcox, S. S. Adler, N. N. Ajitanand, and et al. Suppression of hadrons with large transverse momentum in central  $au + au$  collisions at  $\sqrt{s_{NN}} = 130\text{GeV}$ . *Phys. Rev. Lett.*, 88:022301, Dec 2001.
- [2] Megan Connors, Christine Nattrass, Rosi Reed, and Sevil Salur. Jet measurements in heavy ion physics. *Reviews of Modern Physics*, 90(2), Jun 2018.
- [3] Guang-You Qin and Xin-Nian Wang. Jet quenching in high-energy heavy-ion collisions. *International Journal of Modern Physics E*, 24(11):1530014, Nov 2015.
- [4] Torbjörn Sjöstrand, Stephen Mrenna, and Peter Skands. Pythia 6.4 physics and manual. *Journal of High Energy Physics*, 2006(05):026–026, May 2006.
- [5] J. H. Putschke, K. Kauder, E. Khalaj, and et al. The jetscape framework, 2019.
- [6] [https://commons.wikimedia.org/wiki/File:Standard\\_Model\\_of\\_Elementary\\_Particles.svg](https://commons.wikimedia.org/wiki/File:Standard_Model_of_Elementary_Particles.svg).
- [7] Christian Klein-Bösing. Study of the quark-gluon plasma with hard and electromagnetic probes. <http://qgp.uni-muenster.de/thesisdb/habil-klei-13.pdf>, 2013.
- [8] Yasuo Miake Kohsuke Yagi, Tetsudo Hatsuda. *Quark-Gluon Plasma*. Cambridge University Press, 2005.
- [9] Matthew D. Schwartz. *Quantum Field Theory and the Standard Model*. Cambridge University Press, 2013.
- [10] Christoph Scholz, Bogdan Povh, Werner Rodejohann, Klaus Rith, and Frank Zetsche. *Teilchen und Kerne, 9. Auflage*. Springer Spektrum, 2013.
- [11] Kenneth G. Wilson. Confinement of quarks. *Phys. Rev. D*, 10:2445–2459, Oct 1974.
- [12] A. Bazavov, T. Bhattacharya, M. Cheng, C. DeTar, H.-T. Ding, Steven Gottlieb, R. Gupta, P. Hegde, U. M. Heller, F. Karsch, and et al. Chiral and deconfinement aspects of the qcd transition. *Physical Review D*, 85(5), Mar 2012.
- [13] Wit Busza, Krishna Rajagopal, and Wilke van der Schee. Heavy ion collisions: The big picture and the big questions. *Annual Review of Nuclear and Particle Science*, 68(1):339–376, Oct 2018.
- [14] Gines Martinez. Advances in quark gluon plasma, 2013.

- [15] Johann Rafelski. Connecting qgp-heavy ion physics to the early universe. *Nuclear Physics B - Proceedings Supplements*, 243-244:155–162, Oct 2013.
- [16] M. G. Holloway and C. P. Baker. How the barn was born. *Physics Today*, 25(7):9–9, 1972.
- [17] S. Mandelstam. Determination of the pion-nucleon scattering amplitude from dispersion relations and unitarity. general theory. *Phys. Rev.*, 112:1344–1360, Nov 1958.
- [18] David d’Enterria. 6.4 jet quenching. *Landolt-Börnstein - Group I Elementary Particles, Nuclei and Atoms*, page 471–520, 2010.
- [19] Particle Data Group. Review of Particle Physics. *Progress of Theoretical and Experimental Physics*, 2020(8), 08 2020. 083C01.
- [20] Korinna Zapp. Jewel 2.0.0: directions for use. *The European Physical Journal C*, 74(2), Feb 2014.
- [21] Néstor Armesto, Leticia Cunqueiro, and Carlos A. Salgado. Q-pythia: a medium-modified implementation of final state radiation. *The European Physical Journal C*, 63(4), Sep 2009.
- [22] Kari J. Eskola, Petja Paakkinen, Hannu Paukkunen, and Carlos A. Salgado. Epps16: nuclear parton distributions with lhc data. *The European Physical Journal C*, 77(3), Mar 2017.
- [23] Michael L. Miller, Klaus Reygers, Stephen J. Sanders, and Peter Steinberg. Glauber modeling in high-energy nuclear collisions. *Annual Review of Nuclear and Particle Science*, 57(1):205–243, Nov 2007.
- [24] K. Aamodt, A. Abrahantes Quintana, D. Adamová, et al. Two-pion bose-einstein correlations in central pb–pb collisions at  $\sqrt{s_{NN}}=2.76$  tev. *Physics Letters B*, 696(4):328–337, 2011.
- [25] O. PHILIPSEN. Debye screening in the qcd plasma. *Strong and Electroweak Matter 2000*, Jul 2001.
- [26] Michael Kordell II and Abhijit Majumder. Event-by-event simulations of jet modification using the matter event generator. 02 2017.
- [27] John E. Huth et al. Toward a standardization of jet definitions. In *1990 DPF Summer Study on High-energy Physics: Research Directions for the Decade (Snowmass 90)*, pages 0134–136, 12 1990.
- [28] Matteo Cacciari, Gavin P Salam, and Gregory Soyez. The anti-ktjet clustering algorithm. *Journal of High Energy Physics*, 2008(04):063–063, Apr 2008.



- 
- [29] M Cacciari. <https://www.physics.sjtu.edu.cn/madgraphschoo1/sites/www.physics.sjtu.edu.cn/madgraphschoo1/files/jets2.pdf>.
- [30] Matteo Cacciari, Gavin P. Salam, and Gregory Soyez. Fastjet user manual. 11 2011.
- [31] Leticia Cunqueiro. Jet shapes in pp and pb–pb collisions at alice. *Nuclear Physics A*, 956:593–596, Dec 2016.
- [32] Frédéric A. Dreyer, Gavin P. Salam, and Grégory Soyez. The lund jet plane. *Journal of High Energy Physics*, 2018(12), Dec 2018.
- [33] Andrew J. Larkoski, Simone Marzani, Gregory Soyez, and Jesse Thaler. Soft drop. *JHEP*, 1405:146, 2014.
- [34] Harry Arthur Andrews, Liliana Apolinario, Redmer Alexander Bertens, and et al. Novel tools and observables for jet physics in heavy-ion collisions. 08 2018.
- [35] J. Adam, D. Adamová, M. M. Aggarwal, G. Aglieri Rinella, M. Agnello, N. Agrawal, Z. Ahammed, S. U. Ahn, I. Aimo, and et al. Measurement of jet quenching with semi-inclusive hadron-jet distributions in central pb-pb collisions at  $\sqrt{s_{NN}} = 2.76$  tev. *Journal of High Energy Physics*, 2015(9), Sep 2015.
- [36] S. Agostinelli, J. Allison, K. Amako, and et al. Geant4—a simulation toolkit. *Nuclear Instruments and Methods in Physics Research Section A: Accelerators, Spectrometers, Detectors and Associated Equipment*, 506(3):250–303, 2003.
- [37] S Prestel. <http://home.thep.lu.se/~torbjorn/talks/PrestelSB18.pdf>.
- [38] J. Scott Moreland, Jonah E. Bernhard, and Steffen A. Bass. Alternative ansatz to wounded nucleon and binary collision scaling in high-energy nuclear collisions. *Physical Review C*, 92(1), Jul 2015.
- [39] The ALICE Collaboration. The ALICE experiment at the CERN LHC. *Journal of Instrumentation*, 3(08):S08002–S08002, aug 2008.
- [40] Mrinal Dasgupta, Alessandro Fregoso, Simone Marzani, and Gavin P. Salam. Towards an understanding of jet substructure. *Journal of High Energy Physics*, 2013(9), Sep 2013.
- [41] M. Verweij. Medium modification of jet substructure. [https://indico.cern.ch/event/433345/contributions/2321612/attachments/1411122/2158362/170209\\_JetStructure\\_v3.pdf](https://indico.cern.ch/event/433345/contributions/2321612/attachments/1411122/2158362/170209_JetStructure_v3.pdf).

- [42] Leticia Cunqueiro. Jet production at rhic and lh. <https://indico.cern.ch/event/433345/contributions/2321611/attachments/1411116/2158349/QM17Cunqueiro.pdf>.
- [43] A. Ali and G. Kramer. Jets and qcd: a historical review of the discovery of the quark and gluon jets and its impact on qcd. *The European Physical Journal H*, 36(2):245–326, Sep 2011.
- [44] Simone Marzani, Gregory Soyez, and Michael Spannowsky. Looking inside jets: an introduction to jet substructure and boosted-object phenomenology. *Lecture Notes in Physics*, volume 958 (2019), 01 2019.
- [45] Sevil Salur. A brief review of cms jet measurements. *Journal of Physics: Conference Series*, 589, 03 2015.
- [46] S. Cao, C. Park, R. A. Barbieri, et al. Multistage monte carlo simulation of jet modification in a static medium. *Phys. Rev. C*, 96:024909, Aug 2017.
- [47] Gavin P. Salam. Modification of jet structure in nuclear collisions: theory overview (and pp perspective). *Nuclear Physics A*, 982:149 – 155, 2019. The 27th International Conference on Ultrarelativistic Nucleus-Nucleus Collisions: Quark Matter 2018.

# Acknowledgments

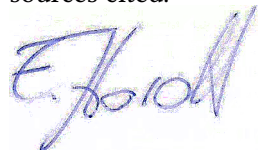
I would like to thank Prof. Dr. Christian Klein-Bösing and Prof. Dr. Anton Andronic for the possibility to create this thesis and all the helpful and interesting physics explanations along the way. Furthermore I would like to thank all the members of the working group

Especially I would like to thank Hendrik Poppenborg, Katharina Garner and Daniel Mühlheim for their help with my physics and programming problems, as well as Philipp Kähler for his thorough editing and Ben Twist and Felix Fidorra for proof reading. I would like to thank Olivia for all the warm words and last but with deepest gratefulness I would like to thank my parents who gave me the opportunity for my studies for their continuous support in this stage of life as well as their lasting patience in all the time it took. *Thank you.*

# Declaration of Academic Integrity

I hereby confirm that this thesis on „Reconstruction of Partonic Substructure and Fragmentation of Jets in Heavy Ion Collisions at the LHC“ is solely my own work and that I have used no sources or aids other than the ones stated.

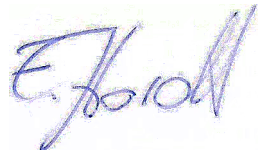
All passages in my thesis for which other sources, including electronic media, have been used, be it direct quotes or content references, have been acknowledged as such and the sources cited.



---

Münster, 8th June 2021 (Fabian Hordt)

I agree to have my thesis checked in order to rule out potential similarities with other works and to have my thesis stored in a database for this purpose.



---

Münster, 8th June 2021 (Fabian Hordt)